

# Implementation of energy transfer technique in ORB5 to study collisionless wave-particle interactions in phase-space.

I. Novikau, A. Biancalani, A. Bottino, A. Di Siena, Ph. Lauber, E. Poli

*Max-Planck-Institut für Plasmaphysik, 85748 Garching, Germany*

E. Lanti, L. Villard, N. Ohana

*École Polytechnique Fédérale de Lausanne, Swiss Plasma Center, Switzerland*

S. Briguglio

*ENEA C.R. Frascati, Via Enrico Fermi 45, CP 65-00044 Frascati, Italy*

---

## Abstract

A new diagnostic has been developed to investigate the wave-particle interaction in the phase-space in gyrokinetic particle-in-cell codes. Keeping information about energy transfer terms in the velocity space, the technique has been implemented and tested in the global code ORB5 and it gives an opportunity to localise velocity domains of maximum wave-plasma energy exchange for separate species. Moreover, contribution of different species and resonances can be estimated as well, by integrating the energy transfer terms in corresponding velocity domains. This Mode-Plasma-Resonance (MPR) diagnostic has been applied to study the dynamics of the Energetic-particle-induced Geodesic Acoustic Modes (EGAMs) in an ASDEX Upgrade shot, by analysing the influence of different species on the mode time evolution. Since the equations, on which the diagnostic is based, are valid in both linear and nonlinear cases, this approach can be applied to study nonlinear plasma effects. As a possible future application, the technique can be used, for instance, to investigate the nonlinear EGAM frequency chirping, or the plasma heating due to the damping of the EGAMs.

---

*Email address: [ivan.novikau@ipp.mpg.de](mailto:ivan.novikau@ipp.mpg.de) (I. Novikau)*

*Keywords:* Gyrokinetics; PIC; Wave-particle interaction; Zonal flows; GAMs; EGAMs

---

## 1. Introduction

Gyrokinetic (GK) codes have recently become standard tools for the investigation of waves and instabilities in tokamak plasmas, with frequency below the ion cyclotron frequency [1]. Although they have been traditionally considered numerically heavy, in comparison to lighter hybrid models, in the last years GK codes have become capable of providing global electromagnetic (EM) predictions of the nonlinear plasma dynamics, thanks to smart schemes improving the numerical performance [2, 3], and to the access to high-performance computers. One advantage of using GK codes is that their model includes kinetic effects such as wave-particle resonances, which are neglected in fluid descriptions.

Wave-particle interaction, such as Landau damping, can be best detected by phase space resolving diagnostics. In particular, investigating collisionless energy transfer signals as a function of particle velocity, necessary details can be provided to identify dominant collisionless processes governing the damping or growth of electrostatic (ES) zonal modes, such as geodesic acoustic modes (GAMs) [4, 5, 6] or energetic-particle driven GAMs, called EGAMs [7, 8, 9, 10]. There are different kind of techniques to investigate dynamics of modes in the phase-space. Correlation techniques [11] can be used to clarify the origin of the energy-transfer process and the nature of mechanisms that lie beyond observed mode dynamics by calculating correlations of the energy transfer terms with different fields signals. Conjunction diagnostics based on the measurements at different positions along the same magnetic flux tube can be used to study the integrated effect of wave-particle interactions between the two space points [12]. The conjunction studies are particularly well suited to study the waves, that are propagating along the magnetic field lines, such as shear-Alfvén waves.

In this work we develop a Mode-Particle-Resonance (MPR) diagnostic in the code ORB5 [13, 14] to investigate energy transfer signals in velocity space

in global gyrokinetic (GK) simulations. The previous version of this diagnostic gave only time evolution of the energy transfer terms, averaged over the whole phase space [15, 16, 17]. We extend it, by keeping information about these terms in the velocity space, that gives an opportunity to investigate the contribution of different resonances in different velocity domains to the mode dynamics. This technique is applied in global GK simulations of an experimental shot on ASDEX-Upgrade machine to study EGAMs. These modes are characterised by the oscillations of mainly toroidally symmetric global radial ES field with frequency comparable to that of the GAMs. The energetic particles (EPs) excite the mode through the inverse Landau damping, and EPs are displaced from higher to lower energy range [18, 19]. On the other hand, the GAMs and EGAMs are mainly damped by Landau damping. In addition to ion Landau damping, GAMs have been found to be subject to the electron Landau damping [20, 21, 22, 23] as well. Here, we show that EGAMs are also subject to electron Landau damping, which can be as important as ion Landau damping in experimentally relevant conditions. Moreover, in these simulations the MPR diagnostic provides additional details to clarify the role of different species in the EGAM-plasma interaction.

The GAMs and EGAMs can play a significant role in the regulation of the turbulence-transport processes. The GAMs are an oscillating branch of zonal flows [24, 5] (ZFs). The ZFs can reduce the radial transport in tokamak plasma acting as a sink for the turbulence energy through the inverse energy cascading or/and by shearing plasma eddies [25, 26, 27, 28]. Contrarily, the role of the GAMs [29, 30, 31, 32] in the turbulence suppression is still unclear and even contradictory [33, 34]. It could be explained by the fact that the GAMs can transfer the energy in both directions. They can either take the energy from the turbulence, being directly excited by instabilities [29] and arising from the ZFs due to the magnetic curvature, or they can return the energy back to the instabilities [33]. Due to this complex dynamics, the role of the EGAMs in the turbulence suppression is still a subject of study [35, 36, 37, 38, 39]. At the same time, EGAMs might play a role of an intermediate agent between the

fluctuating fields and thermal plasma, by spreading fluctuating field energy to the bulk plasma through the collisionless wave-particle interaction [19]. In such a way, the EGAMs might be a crucial component in tokamak plasma stabilisation and be significantly helpful in the plasma heating. Thus, investigation of EGAMs characteristics, especially in the velocity space, is necessary for precise understanding of the transport phenomena in fusion reactors, where the EPs are produced as the result of the nuclear fusion reaction or by external sources such as neutral beam injection (NBI) or ion cyclotron resonance heating (ICRH).

The remainder of the paper is structured in the following way. In section 2 the theoretical background and the implementation of the MPR diagnostic in ORB5 is presented. After that, the processing of the output signals from the diagnostic is demonstrated, and an example of an ES simulation of the GAMs in a circular magnetic configuration is given (Sec. 3). In Sec. 4 we show that the MPR diagnostic verifies the GAM dispersion relation. Having discussed the technique, the experimental AUG shot #31213 is investigated in section 5 using the developed diagnostic in linear simulations. Results, calculated in ORB5, are compared with simulations of the GENE code for an ES case with adiabatic electrons in Sec. 6.

## 2. Formulation and implementation of the Mode-Particle-Resonance diagnostic

### 2.1. Field energy and energy transfer signal

The GK model used in ORB5 is based on a Lagrangian variational principle using a Hamiltonian representation of the perturbed phase-space Lagrangian, which is truncated up to the  $\mathcal{O}(\epsilon_\delta^2)$  terms [17]. Here, the small parameter  $\epsilon_\delta$  is related to the field perturbations and is defined as:

$$\epsilon_\delta = (k_\perp \rho_{th}) \frac{e\Phi}{T_i}, \quad (1)$$

where  $\Phi$  is the ES potential perturbation ( $\mathbf{E} = -\nabla\Phi$ ),  $k_\perp \rho_{th}$  is the normalized perpendicular wavenumber,  $\rho_{th}$  is the thermal ion Larmor radius,  $T_i$  is the

thermal ion temperature. The corresponding ES Hamiltonian contains up to  $\mathcal{O}(\epsilon_\delta^2)$  terms

$$H = H_0 + H_1 + H_2, \quad (2)$$

$$H_0 = \frac{p_z^2}{2m} + \mu B, \quad (3)$$

$$H_1 = ZeJ_0\Phi, \quad (4)$$

$$H_2 = -\frac{mc^2}{2B^2}|\nabla_\perp\Phi|^2. \quad (5)$$

Here,  $m$ ,  $Ze$  are the species mass and charge,  $J_0$  is the gyroaveraging operator Eq. 34,  $p_z$  is a parallel canonical momentum, which is  $p_z = mv_\parallel$  in the ES case,  $\mu$  is the species magnetic moment,  $B$  is the background magnetic field,  $c$  is the light speed. Taking into account the linearised polarization and quasineutrality approximation, which is used in ORB5, the total GK energy in the ES limit has the following form:

$$\mathcal{E} = \sum_{sp} \int dW dV (f(H_0 + H_1) + f_0 H_2) \quad (6)$$

where the kinetic part of the energy is

$$\mathcal{E}_k = \sum_{sp} \int dW dV (f H_0), \quad (7)$$

while the field energy is

$$\mathcal{E}_f = \sum_{sp} \int dW dV (f H_1 + f_0 H_2) \quad (8)$$

Here,  $f(\mathbf{r}, p_z, \mu, t) = f_0(\mathbf{r}, p_z, \mu) + \delta f(\mathbf{r}, p_z, \mu, t)$  is a species distribution function, and the integration is performed over the real  $V$  and velocity  $W$  spaces. Evaluating the time derivative of the kinetic energy  $\mathcal{E}_k$ , the energy transfer between the plasma and the field can be found as

$$\mathcal{P} = \frac{d\mathcal{E}_k}{dt} = - \sum_{sp} Ze \int dV dW f \dot{\mathbf{R}}_0 \cdot \nabla (J_0 \Phi), \quad (9)$$

where  $\dot{\mathbf{R}}_0$  is the species unperturbed equations of motion. The detailed derivation of the GK energy and the plasma-field energy transfer signal can be found in [14, 17].

Finally, it should be noted that the splitting on the 'kinetic' and the 'field' parts is in some sense arbitrary. In this work we keep terms, which depend on species characteristics, in the 'kinetic' part, and the rest of the total energy is taken as the 'field' component. More precisely, using GK Poisson equation, the total energy Eq. 6 can be transformed into the following form Ref. [14]

$$\mathcal{E} = \sum_{sp} \int dW dV \left( \frac{p_z^2}{2m} + \mu B + \frac{1}{2} Z e J_0 \Phi \right) f \quad (10)$$

Here, the first two terms correspond to Eq. 7, while the last term is related to Eq. 8.

## 2.2. Simplified derivation of a wave growth rate

By considering a simplified electrostatic model, we are going to show the derivation of an expression for a wave growth rate. We start from Eq. 9, where due to the energy conservation we can write that

$$\mathcal{P} = \sum_{sp} \mathcal{P}_{sp} = -\frac{d\mathcal{E}_f}{dt}, \quad (11)$$

$$\mathcal{E}_f = \sum_{sp} \frac{m_{sp} c^2}{2B^2} \int dV |\nabla_{\perp} \Phi|^2. \quad (12)$$

Here, the expression for the ES field energy  $\mathcal{E}_f$  is obtained from Eq. 8 and the GK Poisson equation, by treating particles drift-kinetically ( $J_0$  is equal to 1). Considering a general case of a propagating eigenmode and starting from the evolution of the electric field  $\mathbf{E} = -\nabla\Phi$

$$\begin{aligned} \mathbf{E}(\mathbf{r}, t) &= Re [\mathbf{E}(\mathbf{r}) \exp(-i\omega t) \exp(\gamma t)] = \\ &(\cos(\omega t) Re[\mathbf{E}(\mathbf{r})] + \sin(\omega t) Im[\mathbf{E}(\mathbf{r})]) \exp(\gamma t) \end{aligned} \quad (13)$$

where  $\omega$ ,  $\gamma$  are frequency and damping/growth rate of the field, we get an expression for the field energy integrated in space:

$$\mathcal{E}_f(t) = (A^2 + C \cos^2(\omega t)) \exp(2\gamma t), \quad (14)$$

with a constant  $C$  and non-zero constant  $A^2$ . Its time derivative is

$$\frac{d\mathcal{E}_f}{dt} = 2\gamma \mathcal{E}_f - \omega C \sin(2\omega t) \exp(2\gamma t). \quad (15)$$

Using the above equations, we can find the damping/growth rate of the field energy in the following way:

$$\frac{1}{2\mathcal{E}_f} \frac{d\mathcal{E}_f}{dt} = \gamma - \frac{\omega \sin(2\omega t)}{2A^2/C + 1 + \cos(2\omega t)}. \quad (16)$$

Due to the field oscillations, the above expression includes a term, which depends on the field frequency. To exclude this term, one should perform time averaging on several periods of the field oscillations:

$$\int_0^{nT} \frac{\sin(2\omega t)}{2A^2/C + 1 + \cos(2\omega t)} dt = 0, \quad (17)$$

where  $T$  is a period of the field oscillations, and  $n$  is a number of the periods. Due to that, the damping/growth rate of the field can be calculated using the following expression:

$$\gamma = -\frac{1}{2} \frac{1}{nT} \int_0^{nT} \frac{\mathcal{P}}{\mathcal{E}_f} dt, \quad (18)$$

where  $\mathcal{P}$  represents the work done by the ES field on the plasma. A negative rate  $\gamma < 0$  corresponds to a positive signal  $\mathcal{P}$ , indicating the energy transfer from a wave to plasma particles. On the other hand, a positive rate  $\gamma > 0$  corresponds to a growth of the wave. It should be noticed that the GAMs or EGAMs can take the form of a standing wave, which is a limiting case of a propagating wave, where  $2A^2/C \rightarrow \varepsilon$  with a positive infinitesimally small value  $\varepsilon > 0$ :

$$\int_0^{nT} \frac{\sin(2\omega t)}{(1 + \varepsilon) + \cos(2\omega t)} dt = 0. \quad (19)$$

Finally, note that in the case of  $n \neq 0$ , field energy would be a purely growing function that would simplify the problem by exempting us from the time integration in Eq. 18.

### *2.3. Elimination of the zero-frequency zonal flows*

In the previous section, we were assuming that the electric field consists on only an oscillating component, but it can have some residue as well. In case of the zonal electric field, we are dealing with zero-frequency zonal flows (ZFZF).

This constant component might strongly distort the energy transfer and field energy signals, that leads to some errors in the calculation of the GAM damping rate. To estimate the contribution of the ZFZF component, we are going to consider the zonal electric field at some radial point  $s_1$ :

$$e(s_1) = e_0 + e_1 \cos(\omega t) \exp(\gamma t). \quad (20)$$

Here, we assume that the GAM is a standing wave. The field energy, averaged over the whole space, can be expressed in this case as

$$\mathcal{E}_{gam} = \frac{1}{4} E_1^2 (1 + \cos(2\omega t)) \exp(2\gamma t), \quad (21)$$

$$\mathcal{E}_{zf} = \frac{1}{2} E_0^2 + E_0 E_1 \cos(\omega t) \exp(\gamma t) + \mathcal{E}_{gam}, \quad (22)$$

where  $\mathcal{E}_{gam}$  is the field energy of the GAM component,  $\mathcal{E}_{zf}$  is the total energy of the zonal field.  $E_0, E_1$  are amplitudes of the ZFZF and GAM electric field, integrated in space. First of all, we can find the amplitudes  $e_0$  and  $e_1$ , just by averaging in time the signal  $e(s_1)$ . Since we have flat temperature, density and safety factor profiles, we assume that  $e_0$  and  $e_1$  are constant in space. In other words, we can estimate the ZFZF/GAM ratio as

$$\eta = \frac{e_0}{e_1} = \frac{E_0}{E_1}. \quad (23)$$

Using this ratio, we can estimate the GAM contribution to the field energy in the following way

$$E_1^2 = \frac{\mathcal{E}_{zf}(t)}{\frac{1}{2}\eta^2 + \eta \exp(\gamma t) + \frac{1}{2} \exp(2\gamma t)} \Big|_{t=c_n T_{gam}}, \quad (24)$$

where  $T_{gam}$  is a period of the GAM oscillation,  $c_n = 0, 1, \dots$  for  $\eta > 0$  and  $c_n = 1/2, 3/2, \dots$  for  $\eta < 0$ . As a result, one can eliminate the ZFZF contribution to the field energy using the following expression

$$\mathcal{E}_{gam} = \mathcal{E}_{zf} - \eta E_1^2 \left( \frac{1}{2} \eta + \cos(\omega t) \exp(\gamma t) \right). \quad (25)$$

Finally, the energy transfer signal between the GAM and plasma particles can be found as

$$\mathcal{P}_{gam} = -\frac{\partial \mathcal{E}_{gam}}{\partial t} = \mathcal{P}_{zf} + \eta E_1^2 \exp(\gamma t) (\gamma \cos(\omega t) - \omega \sin(\omega t)), \quad (26)$$

$$\mathcal{P}_{zf} = -\frac{\partial \mathcal{E}_{zf}}{\partial t}, \quad (27)$$

where  $\mathcal{P}_{zf}$  is calculated by the MPR diagnostic in ORB5. It must be mentioned that in order to reduce the ZFZF contribution one has to get some preliminary estimation of the GAM frequency and damping rate. Moreover, since in the current version of the MPR diagnostic the energy transfer and field energy signals are averaged in the whole space domain, one can use this diagnostic only in GAM simulations with flat temperature and safety factor profiles, or for the investigation of the EGAM dynamics, whose frequency and growth rate do not change much in radial direction.

#### 2.4. Discretization

To describe the implementation of the diagnostic in the code ORB5, we should start from the discretization of the plasma distribution function in the code. ORB5 is a particle-in-cell (PIC) code, where the Vlasov equation is solved using a Monte Carlo algorithm, and the Maxwell equations are solved using a finite-element method. At the beginning of a simulation a finite collection of initial positions in phase space is sampled by a set of numerical markers [14]. Every marker has a particular magnetic moment  $\mu_{sp} = m_{sp} v_{\perp,sp}^2 / (2B)$ , a position in real space  $\mathbf{R}_{sp}$ , a parallel canonical momentum  $p_{z,sp}$  and it is moving in a background magnetic field  $\mathbf{B} = \mathbf{b}B$  with

$$\mathbf{B}_{sp}^* = \mathbf{B} + \frac{cp_{z,sp}}{Z_{sp}e} \nabla \times \mathbf{b}, \quad (28)$$

$$B_{\parallel,sp}^* = \mathbf{b} \cdot \mathbf{B}_{sp}^*. \quad (29)$$

Here,  $c$  is the speed of light,  $m_{sp}$  and  $Z_{sp}e$  are the species mass and charge, where for electrons  $Z_e e = -e$  and  $e$  is the absolute value of the electron charge. Taking a phase-space position  $Z = (\mathbf{R}_{sp}, p_{z,sp}, \mu_{sp})$  of a species marker as a

random variable, the code distributes the markers in the phase space according to the initial particle distribution function  $f_{0,sp}$ . It means, that each marker is a realisation of the random variable  $Z$ . For simplicity, a marker will be considered as a particle that is moving along a particular orbit defined by the following equations of motion:

$$\dot{\mathbf{R}}_{sp} = \left( \frac{p_{z,sp}}{m_{sp}} - \frac{Z_{sp}e}{m_{sp}c} J_{0,sp} A_{\parallel} \right) \frac{\mathbf{B}_{sp}^*}{B_{\parallel,sp}^*} + \frac{c}{Z_{sp}e B_{\parallel,sp}^*} \mathbf{b} \times [\mu_{sp} \nabla B + Z_{sp}e \nabla (J_{0,sp} \Psi_{sp})], \quad (30)$$

$$\dot{p}_{z,sp} = - \frac{\mathbf{B}_{sp}^*}{B_{\parallel,sp}^*} \cdot [\mu_{sp} \nabla B + Z_{sp}e \nabla (J_{0,sp} \Psi_{sp})], \quad (31)$$

$$\dot{\mu}_{sp} = 0, \quad (32)$$

which are obtained by varying a GK Lagrangian with respect to the phase-space coordinates  $Z = (\mathbf{R}_{sp}, p_{z,sp}, \mu_{sp})$  [17, 40]. The orbits are perturbed by the field perturbation

$$\Psi_{sp} = \Phi - \frac{p_{z,sp}}{m_{sp}c} A_{\parallel}, \quad (33)$$

with  $\Phi$  and  $A_{\parallel}$  being electric and parallel magnetic potential perturbations respectively, where only  $\Phi$  remains in ES simulations. In the gyro-kinetic approximation the code deals with the dynamics of the gyrocentres, whose orbits are perturbed by the potentials, averaged in a space domain, defined by the species Larmor radius, around a marker position. This averaging is represented by the operator  $J_{0,sp}$ :

$$J_{0,sp} G(\mathbf{R}_{sp}, \mu_{sp}) = \frac{1}{2\pi} \int_0^{2\pi} G(\mathbf{R}_{sp} + \boldsymbol{\rho}_{sp}(\alpha)) d\alpha, \quad (34)$$

where  $G(\mathbf{R}_{sp}, \mu_{sp})$  is an arbitrary function, and  $\boldsymbol{\rho}_{sp}$  is the vector going from the guiding center to the particle position. In the drift-kinetic approximation, the potential perturbation is considered at a space point, where a marker is localised, without performing the gyro-averaging. In ORB5 the thermal and fast ions can be treated either gyro-kinetically or drift-kinetically, while the electrons are calculated drift-kinetically.

The time evolution of the plasma distribution function  $f_{sp}$  is described by the Vlasov equation:

$$\frac{df_{sp}}{dt} = \frac{\partial f_{sp}}{\partial t} + \dot{\mathbf{R}}_{\mathbf{sp}} \cdot \nabla f_{sp} + \dot{p}_{z,sp} \frac{\partial f_{sp}}{\partial p_{z,sp}} = 0. \quad (35)$$

Considering perturbations of the distribution function and of the particle orbits till the first order, one can linearize the Vlasov equation:

$$\begin{aligned} & \frac{\partial \delta f_{sp}}{\partial t} + \dot{\mathbf{R}}_{\mathbf{0,sp}} \cdot \nabla \delta f_{sp} + \dot{p}_{0,z,sp} \frac{\partial \delta f_{sp}}{\partial p_{z,sp}} = \\ & - \left( \frac{\partial f_{0,sp}}{\partial t} + \dot{\mathbf{R}}_{\mathbf{0,sp}} \cdot \nabla f_{0,sp} + \dot{p}_{0,z,sp} \frac{\partial f_{0,sp}}{\partial p_{z,sp}} \right) \\ & - \left( \dot{\mathbf{R}}_{\mathbf{1,sp}} \cdot \nabla f_{0,sp} + \dot{p}_{1,z,sp} \frac{\partial f_{0,sp}}{\partial p_{z,sp}} \right). \end{aligned} \quad (36)$$

Assuming that  $f_{0,sp}$  is an equilibrium distribution function, it should be conserved along unperturbed particle trajectories ( $\dot{\mathbf{R}}_{\mathbf{0,sp}}, \dot{p}_{0,z,sp}$ ):

$$\left. \frac{df_{0,sp}}{dt} \right|_0 = \frac{\partial f_{0,sp}}{\partial t} + \dot{\mathbf{R}}_{\mathbf{0,sp}} \cdot \nabla f_{0,sp} + \dot{p}_{0,z,sp} \frac{\partial f_{0,sp}}{\partial p_{z,sp}} = 0. \quad (37)$$

In other words, the first bracket on the right hand side of Eq. 36 is equal to zero. Finally, the time evolution of the perturbation of the species distribution function in linear simulations is described in the following way:

$$\left. \frac{d\delta f_{sp}}{dt} \right|_0 = - \left. \frac{df_{0,sp}}{dt} \right|_1, \quad (38)$$

where  $\left|_1\right.$  indicates that it is necessary to take derivatives along the perturbed parts of species orbits ( $\dot{\mathbf{R}}_{\mathbf{1,sp}}, \dot{p}_{1,z,sp}$ ). Thermal species have an equilibrium distribution function in a form of the Maxwellian one:

$$f_{0,sp}^{therm} = \frac{n_{sp}(\psi)}{(2\pi)^{3/2} u_{th,sp}^3(\psi)} \exp \left[ - \frac{m_{sp}}{T_{sp}(\psi)} \left( \frac{1}{2} \left( \frac{p_{z,sp}}{m_{sp}} \right)^2 + \frac{\mu_{sp} B}{m_{sp}} \right) \right], \quad (39)$$

$$u_{th,sp}(\psi) = \sqrt{\frac{T_{sp}(\psi)}{m_{sp}}}, \quad (40)$$

where  $n_{sp}(\psi)$ ,  $T_{sp}(\psi)$  are species density and temperature profiles along the radial coordinate  $\psi$ , which is the poloidal flux. A symmetric two-bumps-on-tail

distribution function has been used in this work for the fast species [41, 42].

This distribution assumes a flat temperature profile of the fast species:

$$f_{0,sp}^{fast} = A_{sp}(\psi) \exp \left[ -\frac{m_{sp}}{T_{H,sp}} \left( \frac{1}{2} \left( \frac{p_{z,sp}}{m_{sp}} \right)^2 + \frac{\mu_{sp} B}{m_{sp}} \right) - \frac{u_{H,sp}^2}{2T_{H,sp}} \right] \cosh \left( \frac{p_{z,sp}}{m_{sp}} \frac{u_{H,sp}}{T_{H,sp}} \right), \quad (41)$$

$$A(\psi) = \frac{n_{sp}(\psi)}{(2\pi)^{3/2} T_{H,sp}^{3/2}}, \quad (42)$$

where  $u_{H,sp}$ ,  $T_{H,sp}$  are constant input parameters, which specify a shift and width of the bumps respectively.

The perturbation  $\delta f$  is discretized in the  $Z = (\mathbf{R}, p_z, \mu)$  phase space by  $N_{sp}$  markers. Apart of its location  $Z$ , every marker has a particular weight  $w_p(t)$ , which should evolve consistently with the GK Vlasov equation Eq. 35. Here, we omit the index  $sp$  to simplify equations and use the index  $p$ , indicating that a variable is related to a particular marker. Detailed derivation of the weight time evolution can be found in Ref. [13, 14, 43]. A marker weight can be associated to a phase space volume  $\Omega_p$  and correspondent averaged perturbation distribution function  $\langle \delta f \rangle_{\Omega_p}$ :

$$\langle \delta f \rangle_{\Omega_p} = \frac{1}{\Omega_p} \int_{\Omega_p} \delta f \, d\Omega_p = \frac{1}{\Omega_p} \int_{\Omega_p} w_p \delta(\mathbf{R} - \mathbf{R}_p) \delta(p_z - p_{p,z}) \, d\Omega_p, \quad (43)$$

$$w_p(t) = \langle \delta f \rangle_{\Omega_p} \Omega_p, \quad (44)$$

$$\lim_{\Omega_p \rightarrow 0} \langle \delta f \rangle_{\Omega_p} \rightarrow \delta f. \quad (45)$$

Considering uniform spreading of the markers in real space and Maxwellian distribution in the velocity space, it can be shown [43] that the phase space volume  $\Omega_p$ , associated to a marker  $p$ , is

$$\Omega_p = \frac{B_{\parallel,p}^*}{B} v_{\perp,p} (\pi \kappa_v u_{th}(s))^2 \int_0^1 \bar{J}(s) \, ds, \quad (46)$$

where  $\bar{J}(s)$  is the flux-surface-averaged Jacobian,  $\kappa_v$  defines maximum value of the species parallel and perpendicular velocities, normalized to a species thermal speed  $u_{th}(s) = \sqrt{T/m}$ , at every radial point  $s = \sqrt{\psi/\psi_{edge}}$ .

The meaning of the variable  $\Omega_p$  can be explained proceeding directly from the Monte Carlo integration [14]. The expectation value of an arbitrary function  $\zeta(\tilde{Z})$  is

$$E[\zeta(\tilde{Z})] = \int \zeta(z)f(z)dz, \quad (47)$$

where  $\tilde{Z}$  is a random variable, distributed according to the function  $f$ . To minimize the variance of the function  $\zeta$ , one can chose another distribution function  $g(\tilde{Z})$ , which does not vanish in the support of the distribution function  $f$  (so-called importance sampling):

$$E[W(Z)\zeta(Z)] = \int \zeta(z)\frac{f(z)}{g(z)}g(z)dz. \quad (48)$$

In this case, speaking in terms of marker weights and using random variable  $Z$ , distributed with density  $g$ , the expectation value of the function  $\zeta(\tilde{Z})$  is calculated as

$$E[\zeta(\tilde{Z})] = E[W(Z)\zeta(Z)] = \frac{1}{N} \sum_{i=1}^N w(Z_i)\zeta(Z_i), \quad (49)$$

$$w(Z_i) = \frac{f(Z_i)}{g(Z_i)} = f(Z_i)\Omega(Z_i), \quad (50)$$

that is consistent with Eq. 44. In other words, if we have a small amount of markers in a finite phase space volume, their weights will be increased in comparison to a domain where there are higher number of markers at the same phase space volume. More details can be found in Ref. [14].

In the current version of the MPR diagnostic, only the electrostatic part of  $\dot{\mathbf{R}}_{\mathbf{sp}}$  is taken into account. To clarify different terms in Eq. 30, the characteristic

$\dot{\mathbf{R}}_{\mathbf{sp}}$  can be split on the following terms:

$$\dot{\mathbf{R}}_{\mathbf{sp}} = \mathbf{v}_{\parallel,sp} + \mathbf{v}_{\nabla B,sp} + \mathbf{v}_{curvB,sp} + \mathbf{v}_{\nabla p,sp} + \mathbf{v}_{E \times B,sp}, \quad (51)$$

$$\mathbf{v}_{\parallel,sp} = \frac{p_{z,sp}}{m_{sp}} \mathbf{b}, \quad (52)$$

$$\mathbf{v}_{\nabla B,sp} = \mu_{sp} B \frac{1}{Z_{sp} e B_{\parallel,sp}^*} \mathbf{b} \times \frac{\nabla B}{B}, \quad (53)$$

$$\mathbf{v}_{curvB,sp} = \left( \frac{p_{z,sp}}{m_{sp}} \right)^2 \frac{m_{sp}}{Z_{sp} e B_{\parallel,sp}^*} \mathbf{b} \times \frac{\nabla B}{B}, \quad (54)$$

$$\mathbf{v}_{\nabla p,sp} = - \left( \frac{p_{z,sp}}{m_{sp}} \right)^2 \frac{m_{sp}}{Z_{sp} e B_{\parallel,sp}^*} \mathbf{b} \times \left( \mathbf{b} \times \frac{\nabla \times \mathbf{B}}{B} \right), \quad (55)$$

$$\mathbf{v}_{E \times B,sp} = - \frac{\nabla(J_{0,sp} \Phi) \times \mathbf{b}}{B_{\parallel,sp}^*}, \quad (56)$$

where  $\mathbf{b} \times (\nabla \times \mathbf{B})/B = \nabla p/B^2$  in Eq. 55 indicates the dependence on the gradient of the kinetic plasma pressure  $p$ . A precise form of the GK energy transfer signal, valide in both linear and nonlinear cases, can be derived from the GK Hamiltonian using the Noether theorem as it is shown in Ref. [17]:

$$\mathcal{P}_{sp} = -Z_{sp} e \int_V dV \int_{W_{sp}} dW_{sp} (f_{0,sp} + \delta f_{sp}) \dot{\mathbf{R}}_{\mathbf{0,sp}} \cdot \nabla(J_{0,sp} \Phi) \quad (57)$$

with  $V$  and  $W_{sp}$  being real and velocity spaces. The unperturbed particle trajectory  $\dot{\mathbf{R}}_{\mathbf{0,sp}}$  can be obtained from Eq. 51 by eliminating all terms that include the field perturbations  $\Phi$  and  $A_{\parallel}$ . It means, that the term Eq. 56 does not contribute to the energy transfer signal  $\mathcal{P}_{sp}$ . For the equilibrium distribution functions  $f_{0,sp}$ , used in this work (Maxwellian and two bumps-on-tail), the corresponding part of Eq. 57 can be neglected. Because of that, we are going to consider only the term related to  $\delta f_{sp}$ . By integrating the signal over the whole real space  $V$  and in a small velocity domain  $\Delta W_{sp}$ , related to a particular velocity bin, we project the energy transfer signal to the velocity space of a particular species:

$$\mathcal{P}_{sp} = - \frac{Z_{sp} e}{N_{sp}} \sum_{i \in V, \Delta W_{sp}} w_{i,sp} (\mathbf{v}_{i,\parallel,sp} + \mathbf{v}_{i,\nabla B,sp} + \mathbf{v}_{i,curvB,sp} + \mathbf{v}_{i,\nabla p,sp}) \cdot \nabla(J_{0,sp} \Phi)|_i, \quad (58)$$

where the sum  $\sum_{i \in V, \Delta W_{sp}}$  is taken on all markers in the phase volume  $V \Delta W_{sp}$ . The gyro-averaged electric field  $-\nabla(J_{0,sp}\Phi)|_i$  is taken at a position of a marker  $i$ . The sum is normalized to a total number of species markers  $N_{sp}$  in the whole phase-space domain. Since the GK model, that is used in ORB5, is based on the Hamiltonian formulation [17],  $p_{z,sp}$  is used as one of the velocity variables:

$$p_{z,sp} = m_{sp}v_{\parallel,sp} + \frac{Z_{sp}e}{c}J_0A_{\parallel}, \quad (59)$$

This is a common choice in most of the modern GK PIC codes. In the MPR diagnostic a variable  $u_{sp}$  is used for a parallel velocity:

$$u_{sp} = \frac{p_{z,sp}}{m_{sp}}. \quad (60)$$

In the ES case, the variables  $u_{sp}$  and  $v_{\parallel,sp}$  are identical  $u_{sp} = v_{\parallel,sp}$ , and in EM simulations with low  $\beta$  they are close  $u_{sp} \approx v_{\parallel,sp}$ . With the rise of  $\beta$ , the difference between these two variables increases because of the contribution of the parallel magnetic potential  $A_{\parallel}$ . A proper transition from the variable  $p_{z,sp}$  to the variable  $v_{\parallel,sp}$  (instead of  $u_{sp}$ ) is necessary for the investigation of the dynamics of EM modes and for proper analysis of EM simulations. It is a matter of future publications.

### 3. Post-processing

Here, a GAM in a circular magnetic configuration is considered to show how the diagnostic is organised, and how the MPR data are treated. A circular deuterium plasma with flat safety factor  $q = 1.5$ , and flat density and temperature radial profiles is considered. The temperature is defined by the value of  $\rho^* = 1/205$ , where  $\rho^* = \rho_s/a$ , with  $\rho_s = c_s/\omega_{ci}$  and  $c_s = \sqrt{T_e/m_i}$  being the sound speed and  $\omega_{ci} = Z_i e B_0/m_i$  being the ion cyclotron frequency. The simulation has been performed with the electrostatic version of ORB5 with adiabatic electrons. Since here we are interested only in the GAM dynamics, the simulation has been done without energetic species. Non-zonal modes, i.e. modes with toroidal numbers  $n \neq 0$ , have been filtered out to keep only the

physics of the zonal modes. Background magnetic field at the magnetic axis is  $B_0 = 2.0$  T, the minor and major radii are  $a_0 = 0.5$  m,  $R_0 = 1.65$  m respectively. To reduce the computational effort, a radial domain  $s = [0.5, 1.0]$  has been simulated. The radial coordinate is  $s = \sqrt{\psi/\psi_{edge}}$ , where  $\psi$  is the poloidal flux coordinate. The real space has been discretized with  $n_s = 300$  grid points along the radial direction, with  $n_\chi = 64$  along poloidal direction and  $n_\phi = 4$  along toroidal direction. A time step  $dt[\omega_{ci}^{-1}] = 10$  has been chosen, where the time is normalised to the inverse deuterium cyclotron frequency  $\omega_{ci}$ . The number of the ion markers is  $N_i = 10^8$ . To simulate the GAM dynamics, so-called

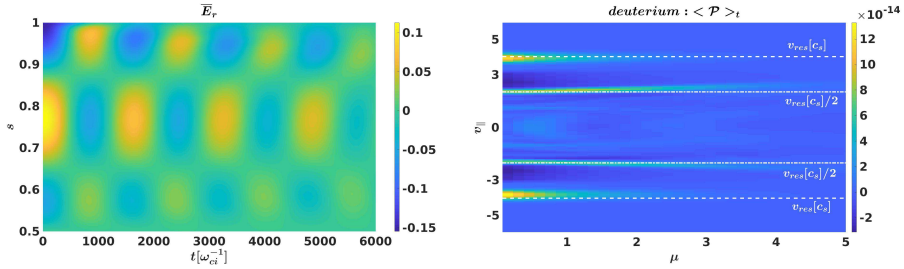


Figure 1: Time evolution of the structure of the GAM radial electric field is shown on the left plot. Velocity dependence of the energy transfer signal, averaged on several GAM periods, is shown on the right plot. White dashed and dotted lines indicate analytical estimation of the parallel velocities where the GAM-plasma resonance should be observed according to the analytical expressions Eq. 61 and Eq. 62. The parallel velocity here is normalized to the sound velocity  $c_s = \sqrt{T_e/m_i}$ , and the magnetic moment is normalized to  $m_i c_s^2 / (2B_0)$ , where  $m_i$  is the deuterium mass.

Rosenbluth-Hinton test [24] has been performed by introducing an axisymmetric density perturbation designed to produce an initial electric potential.

First of all, the MPR diagnostic provides the energy transfer signal  $\mathcal{P}(v_{||}, \mu, t)$  (Eq. 58) as a function of the velocity variables  $(v_{||}, \mu)$  and time. By averaging this signal on several GAM periods, resonances of the mode-particle interaction can be localised in the velocity space. Their location can be compared with the analytically given parallel resonance velocity:

$$v_{||,res} = qR_0\omega_{GAM}, \quad (61)$$

where  $\omega_{GAM}$  is the GAM frequency, that can be found directly from the radial zonal electric field  $\overline{E}_r$ . Since the perturbation of the plasma distribution function related to the GAM dynamics can have higher poloidal modes  $m \geq 1$ , the GAM-particle interaction can be observed at smaller parallel velocities as well

$$v_{\parallel, res}^{(m)} = \frac{qR_0\omega_{GAM}}{m}. \quad (62)$$

By integrating in corresponding velocity domains, one can estimate contribution of these resonances to the mode dynamics. In this particular case, it can be seen from Fig. 1, that the energy transfer occurs mainly at the first resonance  $v_{\parallel, res}$ . By integrating the signal in the whole velocity domain, one gets the time evolution of  $\mathcal{P}$ . By normalizing it to the field energy, the GAM damping rate can be estimated using Eq. 18. Following the algorithm, which has been described in Sec. 2.3, one can eliminate the zero-frequency zonal flow component in the energy transfer and field energy signals. The corresponding signals are shown in Fig. 2.

Eq. 18 involves an integration in time. Varying and choosing different time intervals, one can estimate an errorbar of the GAM damping rate by building a distribution (or histogram) of the damping rate values. Every chosen time interval has to contain a whole (integer) number of GAM periods. The result histogram can be fitted with the normal distribution function, that gives a mean value of the damping rate  $\overline{\gamma}$  and an errorbar is estimated as  $1.96\sigma$ , where  $\sigma$  is the standard deviation, found from the distribution function. The number 1.96 is the 0.975 quantile of the standard normal distribution (Ref. [44]):

$$P(-1.96\sigma < \gamma - \overline{\gamma} < 1.96\sigma) = 0.95, \quad (63)$$

where  $P$  is the probability to find the value of the damping rate in the range  $[\overline{\gamma} - 1.96\sigma, \overline{\gamma} + 1.96\sigma]$ . Here and in the following, including the case with EGAMs, which will be described later, every histogram has 100 or more samples. If the histogram of the damping rate distribution is not fitted by the normal distribution function, one can estimate the calculation error using a more conservative method, by taking the half-width of the area of the damping rate distribution.

A result value of the GAM damping rate, found from the MPR diagnostic is the following:

$$\gamma[\omega_{ci}] = -1.1 \cdot 10^{-4} \pm 1.5 \cdot 10^{-5}, \quad (64)$$

and the distribution of the GAM damping rate values is shown in Fig. 3. Here, values of the errorbar found from the normal distribution function and directly as a half-length of the area of the damping rate distribution are actually the same.

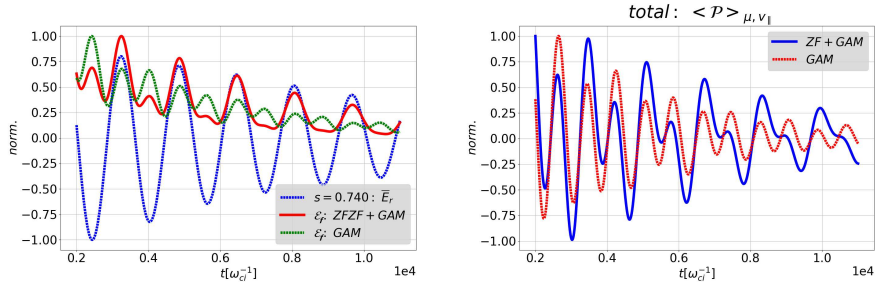


Figure 2: On the left plot, time evolution of the field energy signal with ZFZF and GAM components (red line) and with only GAM component (green line) is plotted. For comparison, the zonal radial electric field at  $s = 0.74$  is shown as well (blue line). On the right plot, the raw energy transfer signal (blue line), which has both ZFZF and GAM components, and the one without the ZFZF component (red line) are presented. The energy transfer signals are averaged over the whole velocity and space domains.

The result from the MPR diagnostic can be compared with the direct calculation of the GAM damping rate, by fitting the zonal radial electric field  $\overline{E}_r$  at a particular radial point. Here, the point  $s = 0.74$  has been taken, since it is very close to a crest in  $\overline{E}_r$ , that can be seen from the left plot of Fig. 1. First of all, the zero-frequency component of  $\overline{E}_r$  is filtered out for more precise calculation of the GAM characteristics. After that, the GAM frequency is estimated, for example, by the Fast Fourier Transform. On the other hand, the damping rate is estimated by the linear least-square root method from the peaks in the time evolution of  $\overline{E}_r$ . This preliminary processing gives the first assumption of the GAM frequency and damping rate, that are used as initial guesses in the

non-linear fitting procedure. A function

$$\sim \cos(\omega t) \exp(\gamma t) \quad (65)$$

is used as a test one, which is fitted to the time evolution of the  $\overline{E}_r(s = 0.74)$ . This method has been used previously in Ref. [22] to study the influence of the drift-kinetic electrons on the GAM dynamics in linear global GK simulations. But here, as in the MPR diagnostic, an opportunity to estimate errorbars of the frequency and especially of the damping (or growth) rate by varying time intervals has been added as well. To exclude outliers during the non-linear fitting, we compare final results with the preliminary estimation of the frequency and damping rate, excluding values, which are significantly different from the preliminary guesses.

Finally, the GAM frequency and damping rate, found using the non-linear fitting of  $\overline{E}_r(s = 0.74)$  to the test function Eq. 65, are the following:

$$\omega[\omega_{ci}] = 3.89 \cdot 10^{-3} \pm 7.8 \cdot 10^{-6}, \quad (66)$$

$$\gamma[\omega_{ci}] = -1.1 \cdot 10^{-4} \pm 8.3 \cdot 10^{-6}, \quad (67)$$

and have been calculated from the corresponding distribution functions, shown in Fig. 3. As it can be seen here, the calculation of the GAM frequency is quite precise with an errorbar being around 0.3%, while the errorbar of the damping rate prediction is around 8%. Comparing both methods (Eq. 64 and 67), one can see that the MPR diagnostic is not as precise as the non-linear fitting, at least, in case of the calculation of the GAM damping rate. On the other hand, it provides additional information such as a position of the GAM-plasma resonances in the velocity space (Fig. 1). Finally, the obtained results can be compared with analytical predictions of the GAM frequency and damping rate, using the Sugama-Watanabe GAM distribution function (Ref. [45, 46]):

$$\omega_{SW}[\omega_{ci}] = 3.98 \cdot 10^{-3}, \quad (68)$$

$$\gamma_{SW}[\omega_{ci}] = -0.8 \cdot 10^{-4}, \quad (69)$$

where it has been taken into account that the GAMs have been initialized with a radial wavenumber  $k_r \rho_i = 8.7 \cdot 10^{-2}$  in a circular plasma system with flat

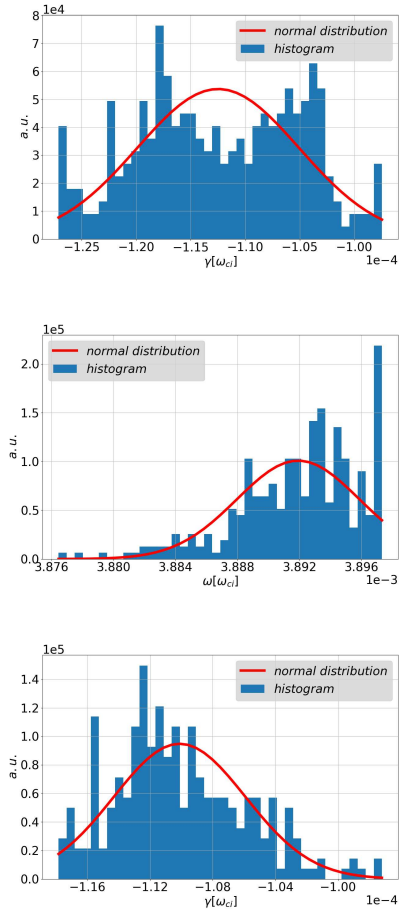


Figure 3: Upper plot: distribution of the GAM damping rate from the MPR diagnostic. Middle and bottom plots: histograms of the GAM frequency and damping rate, found using the non-linear fitting of  $\overline{E}_r(s1)$  to the test function Eq. 65.

safety factor  $q = 1.5$  and temperature  $T_e = T_i = 1.14$  keV profiles. Considering the sensitivity of  $\gamma$  on  $k_r \rho_i$ , the analytical theory gives a good estimation of the GAM damping rate.

#### 4. Analytical verification

Here, we are going to show the consistency of the MPR diagnostic by comparing the GAM measurements investigated with ORB5, with the analytical

dispersion relation derived in the GK framework, by neglecting the effects of the finite Larmor radius and finite orbit width, and considering adiabatic electrons. The corresponding GAM dispersion relation (Ref. [47, 29]) is

$$z + q^2 \left( F(z) - \frac{N^2(z)}{D(z)} \right) = 0, \quad (70)$$

$$N(z) = z + \left( \frac{1}{2} + z^2 \right) \mathcal{Z}(z), \quad (71)$$

$$D(z) = \frac{1}{z} \left( 1 + \frac{1}{\tau_e} \right) + \mathcal{Z}(z), \quad (72)$$

$$F(z) = z \left( z^2 + \frac{3}{2} \right) + \left( z^4 + z^2 + \frac{1}{2} \right) \mathcal{Z}(z), \quad (73)$$

$$\mathcal{Z}(z) = \frac{1}{\sqrt{\pi}} \int_{-\infty}^{+\infty} \frac{\exp(-y^2)}{y - z} dy, \quad (74)$$

$$z = \frac{\hat{\omega}}{\omega_t}, \quad \omega_t = v_{th}/(qR_0), \quad v_{th} = \sqrt{2T/m}. \quad (75)$$

We omit species indices, since all relevant plasma variables are related to the deuterium. A GAM, as a standing wave, is described by the evolution of the zonal electric field:

$$\bar{\mathbf{E}} = (\bar{E}_r, 0, 0), \quad (76)$$

$$\bar{E}_r = E_1 \cos(kr) \exp(-i\hat{\omega}t), \quad (77)$$

with a radial wavenumber  $k$  and a complex frequency  $\hat{\omega} = \omega + i\gamma$ , that verifies the dispersion relation Eq. 70,  $E_1$  is the GAM amplitude. The corresponding perturbation of the deuterium distribution function is (one can find detailed derivation in Appendix A):

$$\delta f = \frac{e}{T} \frac{i\hat{\omega}F_0}{\hat{\omega}^2 - \omega_{tr}^2} \left( \frac{2cT}{eB_0R_0} \frac{N(z)}{D(z)} - v_d \right) \bar{E}_r \sin \theta_p, \quad (78)$$

where  $c$  is the light speed,  $\omega_{tr} = v_{\parallel}/(qR_0)$  is the passing frequency,  $\theta_p$  is the poloidal angle in a simplified circular geometry,  $F_0$  being the deuterium equilibrium distribution function:

$$F_0 = \left( \frac{m}{2\pi T} \right)^{3/2} \exp \left( -\frac{m(v_{\parallel}^2 + v_{\perp}^2)}{2T} \right), \quad (79)$$

and  $v_d$  being the amplitude of the radial drift composed by the curvature drift and grad-B drift:

$$v_d = \frac{mc}{eB_0R_0} \left( \frac{v_\perp^2}{2} + v_\parallel^2 \right). \quad (80)$$

To derive an expression for the energy transfer term, we need the equation of motion Eq. 30, which in a linear ES system can be rewritten as:

$$\dot{\mathbf{R}}_0 = v_\parallel \frac{\mathbf{B}_{sp}^*}{B_{\parallel,sp}^*} + \frac{c\mu}{eB_{\parallel,sp}^*} \mathbf{b} \times \nabla B, \quad (81)$$

where  $\mathbf{B}_{sp}^*$  and  $B_{\parallel,sp}^*$  are defined in Eq. 28 and 29 respectively. Considering a low-pressure plasma ( $\mathbf{J}_0 \times \mathbf{B} \ll 1$  with a plasma current  $\mathbf{J}_0$ ) in a circular plasma cross-section with a curvature  $\boldsymbol{\kappa}$ , one gets the following simplifications:

$$\nabla \times \mathbf{b} = \frac{\nabla \times \mathbf{B}}{B} + \frac{\mathbf{B} \times \nabla B}{B^2} \approx \frac{4\pi}{cB_0} \mathbf{J}_0 + \mathbf{b} \times \boldsymbol{\kappa}, \quad (82)$$

$$\mathbf{J}_0 \cdot \bar{\mathbf{E}} \approx 0, \quad (83)$$

$$\mathbf{b} \times \boldsymbol{\kappa} \cdot \bar{\mathbf{E}} \approx -\frac{\bar{E}_r \sin \theta_p}{R_0}. \quad (84)$$

Applying the introduced approximations, we get that

$$\dot{\mathbf{R}}_0 \cdot \mathbf{E} \approx \dot{\mathbf{R}}_0 \cdot \bar{\mathbf{E}} = -v_d \bar{E}_r \sin \theta_p. \quad (85)$$

Since the energy transfer signal is a real variable, we have:

$$\mathcal{P} = e \int dV dW \mathcal{R}[\delta f] \mathcal{R}[\dot{\mathbf{R}}_0] \cdot \mathcal{R}[\mathbf{E}], \quad (86)$$

and taking into account Eq. 85, one gets:

$$\mathcal{P} = -e \int dV dW \mathcal{R}[v_d \delta f] \mathcal{R}[\bar{E}_r] \sin \theta_p. \quad (87)$$

Considering the integration in velocity and using still complex variables, one obtains that

$$\int dW v_d \delta f = \frac{e}{T} (I_1 - I_2) \bar{E}_r \sin \theta_p, \quad (88)$$

$$I_1 = i\hat{\omega} \frac{2cT}{eB_0R_0} \frac{N(z)}{D(z)} \int \frac{F_0 v_d}{\hat{\omega}^2 - \omega_{tr}^2} dW, \quad (89)$$

$$I_2 = i\hat{\omega} \int \frac{F_0 v_d^2}{\hat{\omega}^2 - \omega_{tr}^2} dW. \quad (90)$$

Evaluating the velocity integrals  $I_1$  and  $I_2$ , one gets the expression

$$I_1 - I_2 = -i \frac{v_{th}^3}{\omega_c^2 R_0} q \left( \frac{N^2(z)}{D(z)} - F(z) \right), \quad (91)$$

which can be significantly simplified using the GAM dispersion relation (Eq. 70) to get rid of the functions  $N(z)$ ,  $D(z)$ , and  $F(z)$ :

$$I_1 - I_2 = -i \frac{v_{th}^2}{\omega_c^2} \hat{\omega}. \quad (92)$$

Using Eq. 87, one can derive an expression for the energy transfer signal:

$$\mathcal{P} = -E_1^2 \frac{mc^2}{B_0^2} (\gamma + \gamma \cos(2\omega t) + \omega \sin(2\omega t)) \exp(2\gamma t) \int dV \sin^2 \theta_p \cos^2(kr). \quad (93)$$

Since we consider the drift-kinetic approximation here, the gyro-averaging operator  $J_0$  is equal to 1. Wave energy is taken from Eq. 12:

$$\mathcal{E}_f = \frac{mc^2}{2B_0^2} \int dV |\nabla_{\perp} \Phi|^2, \quad (94)$$

where we are dealing only with real signals. Finally, taking into account the perturbation of the zonal radial electric field  $|\nabla_{\perp} \Phi|^2 \approx \overline{E_r^2}$  and Since  $\int dW F_0 = 1$ , we get

$$\mathcal{E}_f \approx \frac{mc^2}{4B_0^2} E_1^2 (1 + \cos(2\omega t)) \exp(2\gamma t) \int dV \cos^2(kr). \quad (95)$$

The GAM damping rate can be found using Eq. 18, that leads to the following expression

$$\gamma^{MPR} = 2 \left( \gamma + \frac{\omega}{nT_{gam}} \int \frac{\sin(2\omega t)}{1 + \cos(2\omega t)} dt \right) \frac{\int \cos^2(kr) \sin^2 \theta_p dV}{\int \cos^2(kr) dV}. \quad (96)$$

The ratio of the space integrals is equal to 1/2. Taking into account Eq. 19, we finally can prove the consistency between the GAM dispersion relation and the MPR method:

$$\gamma^{MPR} = \gamma. \quad (97)$$

We can compare the time behaviour of the analytical energy transfer signal Eq. 93 with the corresponding numerical signal. Moreover, we can take into

account the zero-frequency component, as it is done in Eq. 27. If we take the GAM frequency (Eq. 66) and damping rate (Eq. 64 or 67) from the simulation, described in Sec. 3, we can see that the analytical signals show a quite similar behaviour in time (Fig. 4) as the signals from the numerical simulation. The frequency of the  $\mathcal{P}$  signal is double of that of  $\overline{E}_r$ .

The expression Eq. 97 means that using the field and plasma perturbations (Eq. 77 and Eq. 78), which verify the GAM dispersion relation Eq. 70, in the MPR diagnostic (Eq. 18), one gets a GAM damping rate that verifies the original GAM dispersion relation.

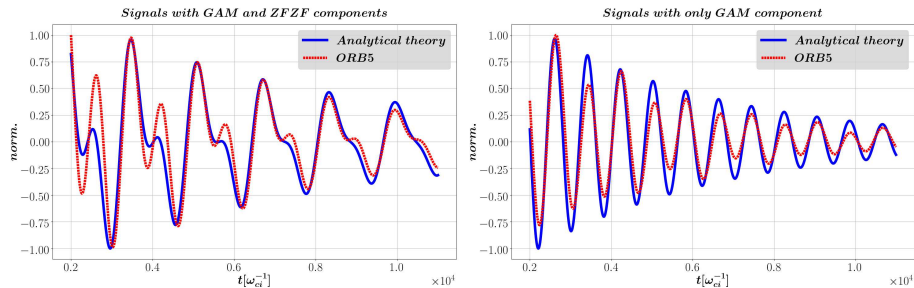


Figure 4: Comparison of the time evolution of the energy transfer signals, obtained from the numerical simulation in Sec. 3 (red dotted lines), and analytically (blue lines) from Eq. 27 (for the left plot) and Eq. 93 (for the right plot). The numerical signal without the zero-frequency zonal flow component, which is shown on the right plot as a red line, has been obtained, using the procedure described in Sec. 2.3.

## 5. Application to EGAMs in AUG shot #31213

### 5.1. Equilibrium and definition of the numerical simulation

The AUG shot #31213 at time 0.84 s has been selected within the Non-Linear Energetic-particle Dynamics (NLED) Eurofusion enabling research project [48, 9]. It has been chosen to study the effect of the energetic particles (EPs) on the dynamics of EGAMs. That is why, in these simulations we have three species: gyro-kinetic thermal deuterium, gyro-kinetic energetic (fast) deuterium, and

thermal electrons, either adiabatic (AE) or drift-kinetic (KE). The linear dynamics of EGAMs in this NLED-AUG case has been recently investigated with the gyrokinetic codes GENE and ORB5 by considering adiabatic electrons [49]. Here, we extend the previous study by investigating the effect of kinetic electrons and describing the contribution of the resonances of all species in phase space. The simulation with the AE is performed in the electrostatic limit, while the simulation with the KE has been done including dynamics of the magnetic potential perturbation as well. In this latter case the pullback method [3] has been used for the mitigation of the cancellation problem in EM simulations [50, 2]. Corresponding profiles of the safety factor, species density and temperature are shown in Fig. 5. The magnetic field is reconstructed with experimental data, including all geometrical effects (Fig. 5). The magnetic field at the magnetic axis is  $B_0 = 2.2$  T. The major radius at the axis is  $R_0 = 1.67$  m. The geometrical major and minor radii are  $R_0 = 1.62$  m,  $a = 0.482$  m respectively. The

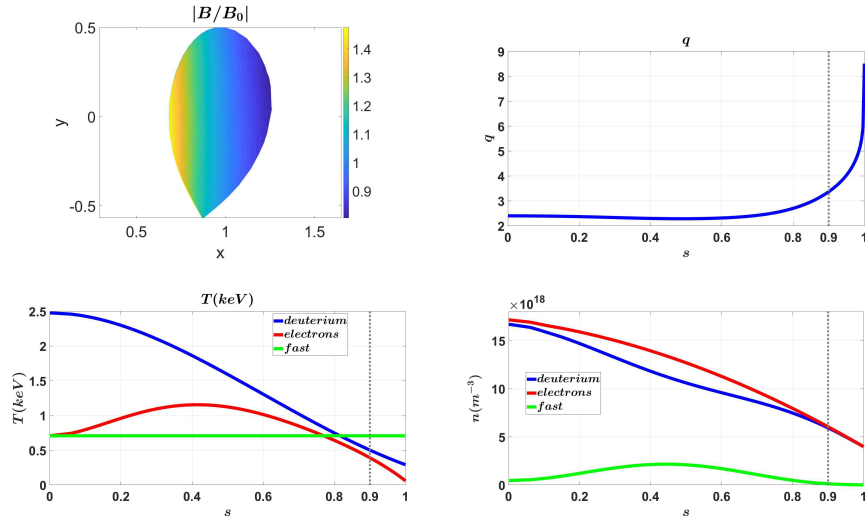


Figure 5: Magnetic configuration (upper left plot), radial profile of the safety factor (upper right plot), species temperature (lower left plot) and density (lower right plot) radial profiles for the EGAM simulations in the ASDEX Upgrade shot #31213. The grey vertical dotted lines indicate the right boundary of the simulated radial domain in the EM case with drift-kinetic electrons.

real space of the system has been discretized using the following parameters:  $n_s = 256$ ,  $n_\chi = 256$ ,  $n_\phi = 32$ . In the ES simulation the time grid has a step  $dt[\omega_{ci}^{-1}] = 20$  with  $N_i = 5 \cdot 10^8$  being a number of markers for the thermal ions, and  $N_f = 5 \cdot 10^8$  for the fast ions. In the EM case, the time step and number of markers have been changed:  $dt[\omega_{ci}^{-1}] = 5$ ,  $N_i = N_f = 10^8$ ,  $N_e = 4 \cdot 10^8$ . Such a high number of markers is needed to provide at least several thousands of numerical markers in every velocity bin, where the mode-plasma resonances are observed (Fig. 6). In the EM case the radial domain has been reduced to  $s = [0.0, 0.9]$  to avoid numerical instabilities due to the abrupt increase of the safety factor at the edge. The density profile, that is depicted in Fig. 5, corresponds to the case with  $\beta_e = \langle n_e \rangle T_e / (B_0^2 / (2\mu_0)) = 2.7 \cdot 10^{-4}$ , where  $\langle n_e \rangle$  is the electron density, averaged in a tokamak volume,  $\mu_0$  is the magnetic constant, and  $T_e$  is measured at the radial position  $s = 0.0$ . In both cases, the velocity distribution of the fast particles is described by the expression Eq. 41 with  $u_{H,f} = 8$  and  $T_{H,f} = 1$ . It means that the distribution function of the fast species is centred around  $v_{\parallel} = 8$  and  $v_{\parallel} = -8$  (two bumps-on-tail), as one can see from Fig. 10 (grey line). Due to this shift in the parallel velocity, the fast particles lie near the EGAM-particle resonance velocity, which is estimated in Eq. 62, and can exchange energy with the radial electric field. More precisely, the fast deuterium particles, which lie on the positive slope of the right bump and negative slope of the left bump, in total, transfer their energy to the electric field, driving in such a way the EGAMs. The width of these bumps is constant in space, which is described by the flat temperature profile of the fast species. The distribution function with two symmetric bumps-on-tail, but not only with one bump, is used to avoid input of additional momentum into the plasma system, which can change the GAM frequency, and as a result, shift the position of the resonance between the EGAM and fast species. The term "fast" is used to identify species which are responsible for the EGAM excitation. The ORB5 simulation with such parameters of the fast species results in one of the highest EGAM growth rate for the given plasma configuration.

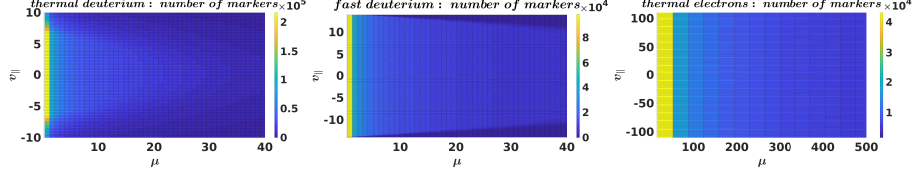


Figure 6: Distribution of the numerical markers among velocity bins for different species. The parallel velocity here is normalized to the sound velocity  $c_s = \sqrt{T_{e,max}/m_i}$ , and the magnetic moment is normalized to  $m_i c_s^2 / (2B_0)$ , where  $T_{e,max}$  is the maximum electron temperature,  $m_i$  is the thermal ion (deuterium) mass.

### 5.2. Numerical investigation of the wave-particle resonances in the EGAM dynamics

First of all, one can notice from Fig. 7 that the radial structure of the EGAMs slightly changes when the dynamics of the drift-kinetic electrons is switched on. The position of the crest in the EGAM radial structure shifts inwards from around  $s = 0.48$  to  $s = 0.40$ . Considering firstly the ES case with AE, we

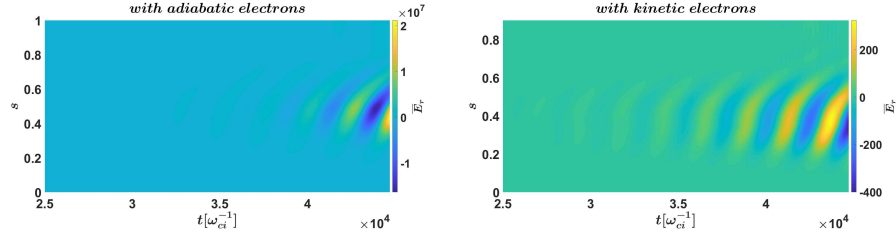


Figure 7: Comparison of the radial structure of  $\bar{E}_r$  in simulations with adiabatic (left plot) and drift-kinetic (right plot) electrons.

compare the EGAM frequency and growth rate, calculated at radial positions  $s = 0.40$  and  $s = 0.48$ , using the non-linear fitting of  $\bar{E}_r$ :

$$s = 0.40 : \quad \omega[\sqrt{2}v_{th,i}/R_0] = 9.391 \cdot 10^{-1} \pm 3.5 \cdot 10^{-4}, \quad (98)$$

$$\gamma[\sqrt{2}v_{th,i}/R_0] = 1.63 \cdot 10^{-1} \pm 1.4 \cdot 10^{-3}, \quad (99)$$

$$s = 0.48 : \quad \omega[\sqrt{2}v_{th,i}/R_0] = 9.314 \cdot 10^{-1} \pm 3.7 \cdot 10^{-4}, \quad (100)$$

$$\gamma[\sqrt{2}v_{th,i}/R_0] = 1.65 \cdot 10^{-1} \pm 1.4 \cdot 10^{-3}. \quad (101)$$

From here on, only the radial point  $s = 0.40$  is considered in the following calculations. Consistency between the EGAM growth rate, calculated directly from  $\bar{E}_r$  and by the MPR diagnostic, using Eq. 18, significantly improves in time due to the growth of the EGAM signal in comparison with the zero-frequency zonal flow. Skipping initial transient time period, the MPR diagnostic can be applied to measure the EGAM growth rate, that appears to be consistent with Eq. 99:

$$MPR : \gamma[\sqrt{2}v_{th,i}/R_0] = 1.63 \cdot 10^{-1} \pm 2.8 \cdot 10^{-3}. \quad (102)$$

The consistency between both methods is observed in the EM case with KE as well:

$$\bar{E}_r(s = 0.4) : \quad \omega[\sqrt{2}v_{th,i}/R_0] = 9.586 \cdot 10^{-1} \pm 4 \cdot 10^{-4}, \quad (103)$$

$$\bar{E}_r(s = 0.4) : \quad \gamma[\sqrt{2}v_{th,i}/R_0] = 8.5 \cdot 10^{-2} \pm 1.0 \cdot 10^{-3}, \quad (104)$$

$$MPR : \quad \gamma[\sqrt{2}v_{th,i}/R_0] = 8.4 \cdot 10^{-2} \pm 3.6 \cdot 10^{-3}. \quad (105)$$

From Eq. 98 and Eq. 103 one can see that the change in the EGAM frequency is small in comparison with the change in the growth rate, when dynamics of the drift-kinetic electrons is included. In particular, the EGAM growth rate decreases from Eq. 102 to Eq. 105. We now want to investigate the role of the drift-kinetic electrons in the EGAM dynamics to understand which wave-particle interactions lead to the decrease of the EGAM total growth rate, by estimation of the contribution of different species. In the simulation with adiabatic electrons:

$$thermal\ deuterium : \quad \gamma[\sqrt{2}v_{th,i}/R_0] = -2.99 \cdot 10^{-1} \pm 3.9 \cdot 10^{-3}, \quad (106)$$

$$fast\ deuterium : \quad \gamma[\sqrt{2}v_{th,i}/R_0] = 4.62 \cdot 10^{-1} \pm 2.3 \cdot 10^{-3}. \quad (107)$$

These equations show that the total EGAM growth rate is a balance between the drive on the fast species and damping on the thermal one (one can see also Ref. [42] for a similar analysis in the case of EGAMs in simplified configurations, with adiabatic electrons). Moreover, the absolute values of the species contri-

butions are much higher than the absolute value of the EGAM total growth rate.

In case with drift-kinetic electrons, the species contributions are the following:

$$\textit{thermal deuterium} : \quad \gamma[\sqrt{2}v_{th,i}/R_0] = -3.94 \cdot 10^{-1} \pm 4.1 \cdot 10^{-3}, \quad (108)$$

$$\textit{thermal electrons} : \quad \gamma[\sqrt{2}v_{th,i}/R_0] = -2.67 \cdot 10^{-2} \pm 4.6 \cdot 10^{-4}, \quad (109)$$

$$\textit{fast deuterium} : \quad \gamma[\sqrt{2}v_{th,i}/R_0] = 5.03 \cdot 10^{-1} \pm 4.7 \cdot 10^{-3}. \quad (110)$$

From the above equations one can see that the drive on the fast particles (Eq. 107 and 110) and damping on the thermal ions (Eq. 106 and 108) increase with the inclusion of the electron dynamics. Since this increase is comparable with the electron contribution (Eq. 109), one cannot claim from these results that the decrease of the EGAM growth rate occurs only directly due to the additional damping on electrons.

But apart of that, the inclusion of drift-kinetic electrons changes the position of the EGAM crest (Fig. 7) and slightly changes the EGAM frequency. These changes can lead to the observed increase of the thermal and fast ions contribution to the EGAM drive. Nevertheless, it is clearly shown here that in the experimentally relevant plasma conditions the inclusion of the drift-kinetic electrons significantly decreases the EGAM growth rate of about a factor 2.

We now want to investigate the role of the different resonances in phase space. In Fig. 8b one can see the energy transfer signal for the EGAM-electron interaction in the velocity space, averaged on several EGAM periods. The red cone there indicates an analytical estimation of the boundary between the passing and trapped electrons:

$$v_{\parallel}^{p-tr} = \sqrt{2\epsilon\mu}, \quad (111)$$

where  $\epsilon$  is an inverse aspect ratio. According to that figure, the EGAMs are damped by the electrons which are localised mainly near this boundary, similar to what happens for GAMs [20]. We should mention here that the estimated localisation of the passing-trapped boundary is shown in Fig. 8b only as a guide

for the eye, and it is not used during the actual GK simulations. We can separate three different velocity domains  $e1$ ,  $e2$ ,  $e3$ . The area  $e1$ , which is between the passing-trapped boundary and a white parabola in Fig. 8b, describes mostly the contribution of the barely trapped electrons to the EGAM damping. The area  $e2$ , which is inside of the white parabola, corresponds to the deeply trapped electrons. Finally, the area  $e3$ , that is the velocity domain outside the passing-trapped boundary, describes the passing electrons. By averaging, for example, in the velocity domain  $e1$ , one gets the time evolution of the energy transfer signal (Fig. 8a), that should be filtered for its proper use in Eq. 18. The contributions of the electrons from different velocity domains are the following:

$$e1 : \quad \gamma[\sqrt{2}v_{th,i}/R_0] = -1.37 \cdot 10^{-2} \pm 3.9 \cdot 10^{-4}, \quad (112)$$

$$e2 : \quad \gamma[\sqrt{2}v_{th,i}/R_0] = 2.5 \cdot 10^{-3} \pm 2.0 \cdot 10^{-4}, \quad (113)$$

$$e3 : \quad \gamma[\sqrt{2}v_{th,i}/R_0] = -1.47 \cdot 10^{-2} \pm 2.3 \cdot 10^{-4}, \quad (114)$$

$$e1 + e2 + e3 \approx -2.59 \cdot 10^{-2}. \quad (115)$$

In Fig. 9 one can see more precisely the energy flow between the zonal electric field and the electrons in different velocity domains. First of all, we would like to notice that one of the dominant component to the electron damping occurs due to the barely trapped electrons ( $e1$ ). It is reasonable since the resonant velocity of the EGAM-electron interaction lies in the domain of the barely trapped particle. On the other hand, we can see a significant contribution of passing electrons to the EGAM damping Eq. 114. The reason might be in the choice of the velocity space variables in ORB5, which has been explained in Sec. 2 in Eq. 59. More precisely, we have some contribution of the parallel magnetic potential to the velocity coordinate, used in the MPR diagnostic. To reduce this component, we can decrease the plasma  $\beta$ , as it is done in Appendix C that leads to smaller contributions of passing and deeply trapped electron in the field-electron interaction, keeping the same damping on barely trapped electrons.

We can estimate as well contribution of different resonances in the thermal

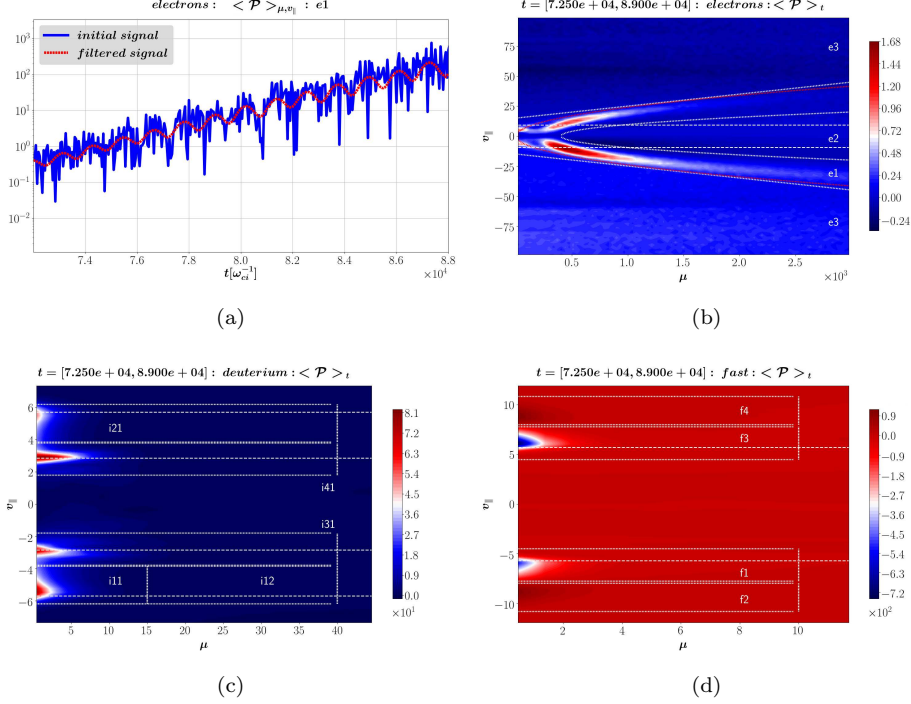


Figure 8: Upper right plot: the energy transfer signal, averaged on several EGAM periods, is shown with indication of different velocity domains, where the electron contribution to the EGAM dynamics is investigated. The red cone indicates the analytical estimation of the passing-trapped boundary Eq. 111. The main EGAM-electron interaction is observed in the domain  $e1$ , which is between the passing-trapped boundary and the white dotted parabola. The white horizontal dashed lines indicate the analytical estimation of the main EGAM-plasma resonance Eq. 61. Upper left plot: energy transfer signal, averaged in the velocity domain  $e1$ . The blue line corresponds to the initial raw signal, while the red line shows the signal, after low-pass filtering. Bottom row: the energy transfer signals for the thermal (left plot) and fast (right plot) deuterium with indication of different velocity domains. The dotted lines indicate positions of the first  $v_{||,res}$  and second  $v_{||,res}/2$  resonances. The parallel velocity here is normalized to the sound velocity  $c_s = \sqrt{T_{e,max}/m_i}$ , and the magnetic moment is normalized to  $m_i c_s^2 / (2B_0)$ , where  $T_{e,max}$  is the maximum electron temperature,  $m_i$  is the mass of the thermal deuterium.

deuterium velocity space (Fig. 8c):

$$i11 : \quad \gamma[\sqrt{2}v_{th,i}/R_0] = -1.01 \cdot 10^{-1} \pm 3.4 \cdot 10^{-3}, \quad (116)$$

$$i12 : \quad \gamma[\sqrt{2}v_{th,i}/R_0] = -1.02 \cdot 10^{-1} \pm 3.7 \cdot 10^{-3}, \quad (117)$$

$$i21 : \quad \gamma[\sqrt{2}v_{th,i}/R_0] = -6.7 \cdot 10^{-2} \pm 2.7 \cdot 10^{-3}, \quad (118)$$

$$i31 : \quad \gamma[\sqrt{2}v_{th,i}/R_0] = -9.6 \cdot 10^{-2} \pm 2.6 \cdot 10^{-3}, \quad (119)$$

$$i41 : \quad \gamma[\sqrt{2}v_{th,i}/R_0] = -1.00 \cdot 10^{-1} \pm 1.4 \cdot 10^{-3}, \quad (120)$$

$$i12 + i21 + i31 + i41 \approx -3.65 \cdot 10^{-1}, \quad (121)$$

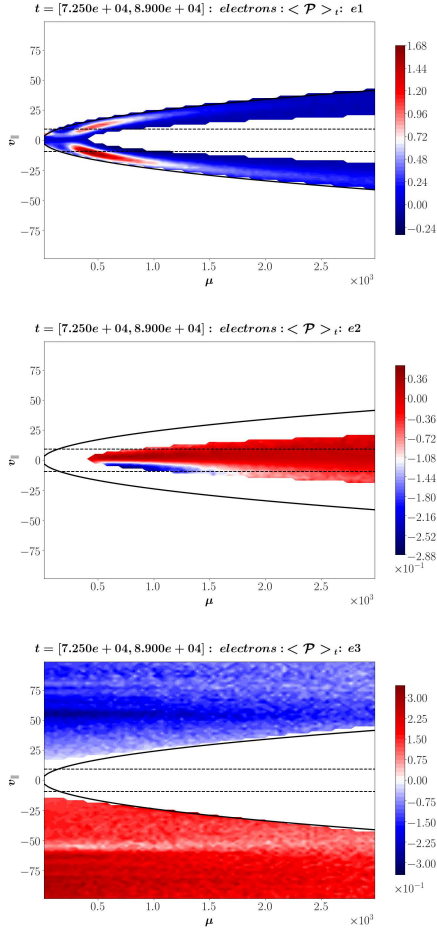


Figure 9: Energy transfer between the EGAM and the thermal electrons, averaged on several EGAM periods, in different velocity domains, which are indicated in Fig. 8b. The black cone is the electron passing-trapped boundary. The dashed horizontal lines are the analytical estimation of the main resonant velocities.

where the domain  $i21$  is the same as  $i11$ , but extended along  $\mu$ .

In Eq. 121 the contributions of all considered resonances are summed up. The result value is close enough to the total contribution of the thermal ions to the EGAM damping (Eq. 108). From one point of view, it is an additional option to verify the implemented diagnostic. On the other hand, by comparing Eq. 116 and 117, one can see that the parallel dynamics has a predominant contribution

to the energy exchange between the EGAMs and the thermal deuterium plasma.

Finally, we can consider different velocity domains in the EGAM - energetic deuterium interaction (Fig. 8d):

$$f1 : \quad \gamma[\sqrt{2}v_{th,i}/R_0] = 2.85 \cdot 10^{-1} \pm 4.78 \cdot 10^{-3}, \quad (122)$$

$$f2 : \quad \gamma[\sqrt{2}v_{th,i}/R_0] = -7.11 \cdot 10^{-2} \pm 3.8 \cdot 10^{-3}, \quad (123)$$

$$f3 : \quad \gamma[\sqrt{2}v_{th,i}/R_0] = 3.61 \cdot 10^{-1} \pm 6.3 \cdot 10^{-3}, \quad (124)$$

$$f4 : \quad \gamma[\sqrt{2}v_{th,i}/R_0] = -6.7 \cdot 10^{-2} \pm 4.0 \cdot 10^{-3}, \quad (125)$$

$$f1 + f2 + f3 + f4 = 5.08 \cdot 10^{-1}. \quad (126)$$

One can see that there is an EGAM damping even on the energetic particles (Eq. 123 and 125). But it is significantly smaller than the dominant drive (Eq. 122 and 124). Sum on the resonances (Eq. 126) indicates that the EGAMs are driven by the fast species and its absolute value is close enough to the total drive, found in Eq. 110.

## 6. Comparison with GENE

To verify some of the results, obtained in Sec. 5, we have performed a comparison with the gyrokinetic GENE code, that has a similar diagnostic. The Gyrokinetic Electromagnetic Numerical Experiment (GENE) [51] is an Eulerian code, which solves the Vlasov-Maxwell system of coupled equations on the phase-space grid  $(\mathbf{R}, v_{\parallel}, \mu)$  at each time step. Here,  $\mathbf{R}$  denotes the gyrocenter position,  $v_{\parallel}$  the velocity component parallel to the magnetic field and  $\mu$  the magnetic moment. The gyrokinetic description employs an approach based on the study of a distribution function  $f_s(\mathbf{R}, v_{\parallel}, \mu)$  for each plasma species ( $s$ ), which contrarily as it is done in a particle-in-cell code as ORB5, is not discretized with markers. The distribution function is split, accordingly to the so-called  $\delta$ -f approach, into a background component  $f_{0,s}$  and in a small fluctuating part  $f_{1,s}$ , i.e.  $f_s = f_{0,s} + f_{1,s}$ . The equilibrium distribution function  $f_{0,s}$  is usually modelled with a Maxwellian distribution. However, recently, this assumption has been relaxed and more flexible equilibrium distributions can

be considered [52, 53, 54]. In particular, different analytic choices, e.g. slowing down, bi-Maxwellian and bump-on-tail, as well as numerical distributions as obtained from numerical models are supported. While the equilibrium distributions are considered time independent on the turbulent time scales, their perturbed components evolve in time accordingly to the Vlasov equation, which in the linear and electrostatic limit employed throughout this paper reads as (for more details one can see Ref. [55, 56, 57])

$$\begin{aligned} \frac{\partial f_{1,s}}{\partial t} + \frac{\mathcal{C}v_{th,s}}{2\mathcal{J}B_0} \left[ v_{\parallel}^2 + \mu B_0, h_{1,s} \right]_{zv_{\parallel}} + \frac{1}{\mathcal{C}} \frac{\partial \bar{\phi}_1}{\partial y} \partial f_{0,s} \\ + \frac{T_0}{q_s} \frac{2v_{\parallel}^2 + \mu B_0}{B_0} \left( \mathcal{K}_x \frac{\partial h_{1,s}}{\partial x} + \mathcal{K}_y \frac{\partial h_{1,s}}{\partial y} \right) = 0. \end{aligned} \quad (127)$$

Here, the function  $h_{1,s}$  represents the non-adiabatic part of the perturbed distribution function  $f_{1,s}$ . It is defined as  $h_{1,s} = f_{1,s} - q\bar{\phi}_1/(B_0 T_{0,s}) \partial f_{0,s} / \partial \mu$ . Eq. 127 is written in the field aligned coordinate system  $(x, y, z)$  with  $x$  the radial,  $y$  the bi-normal and  $z$  the field aligned directions. Moreover,  $\bar{\phi}_1$  denotes the gyro-averaged electrostatic potential,  $\mathcal{J}$  the phase-space jacobian,  $\mathcal{K}_x \sim -\partial_y B_0 - \partial_z B_0$  and  $\mathcal{K}_y \sim \partial_x B_0 - \partial_z B_0$ , respectively, the radial and bi-normal curvature terms and  $\mathcal{C}^2 = \mathbf{B}_0 \cdot \mathbf{B}_0$ . Finally, the Poisson brackets are defined as

$$[a, b]_{c,d} = \frac{\partial a}{\partial c} \frac{\partial b}{\partial d} - \frac{\partial a}{\partial d} \frac{\partial b}{\partial c}. \quad (128)$$

Eq. 127 needs to be solved self-consistently with the Poisson field equation. The full plasma dynamic can be investigated in GENE either in a flux-tube (local assumption) [51] or in a full-global radial domain [55]. The local approximation allows the radial direction to be Fourier transformed by assuming periodic boundary conditions. GENE is able to study the contribution of each plasma species to the overall more unstable mode-dynamic through the study of the time evolution of the potential energy of the system  $E_w$  [58, 59]. It is defined only in Fourier space (only in the local flux-tube limit) for each wave vector  $\mathbf{k} = (k_x, k_y)$  as follows

$$E_w = \left\langle \int d\mu dv_{\parallel} \frac{\pi}{2} B_0 n_0 q \bar{\Phi}_{1,k}^* f_{1,k} \right\rangle_z. \quad (129)$$

Here, the bracket represents the field-aligned z-average, namely

$$\langle A(z) \rangle_z = \frac{\int \mathcal{J}(z) A(z) dz}{\int \mathcal{J}(z) dz}. \quad (130)$$

The time derivative of Eq. 129 determines the energy flow during the whole simulation time domain. In particular it represents the energy effectively transferred from the particles to the field. It reads as

$$\frac{\partial E_w}{\partial t} = \left\langle \int d\mu dv_{\parallel} \frac{\pi}{2} B_0 n_0 q \bar{\Phi}_{1,k}^* \partial_t f_{1,k} \right\rangle_z. \quad (131)$$

From the energy relation of Eq. 131 it is to compute the more unstable linear growth rate  $\gamma$  through the time variation of the potential energy, as shown in details in Ref [49, 15, 58, 60], by the relation

$$\gamma = \frac{1}{E_w} \sum_s \frac{\partial E_{w,s}}{\partial t}. \quad (132)$$

Eq. 132 allows us to distinguish between the contribution of each species to the total growth rate, by removing the sum over all the species and studying each term separately. Positive (negative) values of  $\partial E_{k,s}/\partial t$  indicate that the plasma species considered is giving (taking) energy to (from) the electrostatic field component with a consequent growth (damping) of the mode. Moreover, by studying  $\gamma_s$  in phase-space, i.e.  $(v_{\parallel}, \mu)$  for each plasma species, velocity resonances, which are the main drive term of the EGAMs studied in this paper, can be investigated in details.

The same AUG shot has been simulated in GENE in case with adiabatic electrons (one can see also Ref. [49]), using the flux-tube version of the code at  $s = 0.5$ . In Fig. 10 one can see that both ORB5 and GENE give the same positions of the resonances of the EGAM - fast deuterium plasma interaction. According to chosen parameters of the fast deuterium distribution function, peaks of the energetic bumps are located at  $|v_{\parallel}| = 8$ . As a benchmark, comparison of the EGAM frequency and total growth rate has been done as well. One can see that both codes give the same values of the mode frequency:

$$GENE : \quad \omega/2\pi = 42 \text{ (kHz)}, \quad (133)$$

$$ORB5 : \quad \omega/2\pi = 43.60 \pm 0.02 \text{ (kHz)}. \quad (134)$$

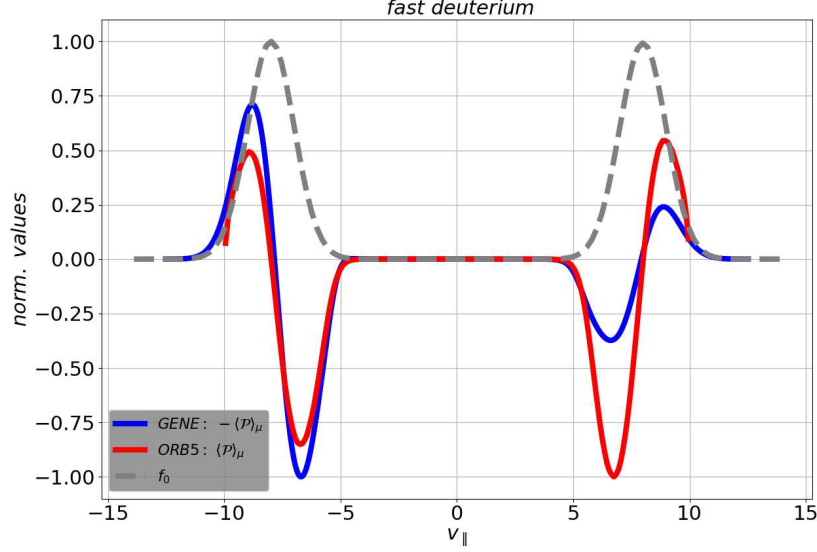


Figure 10: Resonance positions of the EGAM - fast deuterium interaction, obtained from GENE and ORB5. The velocity grid is normalised to the sound speed  $c_s = \sqrt{T_{e,max}/m_i}$ . The grey dotted line indicates the positions of the bumps, which describe the equilibrium distribution of the fast deuterium.

On the other hand, there is 18% consistency between the codes for the EGAM total growth rate:

$$GENE : \quad \gamma = 40 \cdot 10^3 \text{ (s}^{-1}\text{)}, \quad (135)$$

$$ORB5 : \quad \gamma = (47.6 \pm 0.4) \cdot 10^3 \text{ (s}^{-1}\text{)}, \quad (136)$$

and for the contributions of different plasma species to the mode dynamics:

$$thermal \ deuterium : \quad GENE : \gamma = -74 \cdot 10^3 \text{ (s}^{-1}\text{)}, \quad (137)$$

$$ORB5 : \gamma = (-87 \pm 1) \cdot 10^3 \text{ (s}^{-1}\text{)}, \quad (138)$$

$$fast \ deuterium : \quad GENE : \gamma = 115 \cdot 10^3 \text{ (s}^{-1}\text{)}, \quad (139)$$

$$ORB5 : \gamma = (134.8 \pm 0.7) \cdot 10^3 \text{ (s}^{-1}\text{)}. \quad (140)$$

The difference in the values can be explained mainly by the fact that the

simulation in GENE has been performed using the local flux-tube version, while the simulation in ORB5 is a global one.

## 7. Conclusions

In this paper a Mode-Particle-Resonance (MPR) diagnostic has been implemented in the gyrokinetic code ORB5 to investigate mode-plasma interaction processes. The technique is based on the investigation of energy transfer terms in the velocity space (Eq. 58) and gives an opportunity to localise velocity domains of maximum energy exchange between an electrostatic mode and different species.

Moreover, integrating in a chosen velocity domain, a rate of the mode damping or growth can be calculated using Eq. 18 and contribution of different species to the mode dynamics can be estimated as well. Using a GAM dispersion relation, which neglects finite-Larmor-radius and finite-orbit-width effects and treats the electrons as adiabatic [47, 29], the theoretical principle, which lies behind the MPR diagnostic, has been analytically verified for an ES case. It has been shown that the GAM damping rate, derived from the energy exchange principle (Eq. 18), is identical to the GAM damping rate, given by the GAM dispersion relation Eq. 70. Analytical time evolution of the energy transfer signal, given in Eq. 93, has been found to have the same frequency as the numerical one (Fig. 4).

In Sec. 5, the MPR diagnostic has been applied to the case of AUG shot #31213 (NLED AUG base case) to investigate contributions of different resonances to the EGAM dynamics. It has been shown that inclusion of the drift-kinetic electrons significantly decreases the EGAM growth rate of about a factor 2 for the selected case (Eq. 102 and Eq. 105). It has been shown that the EGAM damping occurs at the first and second resonances in case of the interaction with deuterium plasma. On the other hand, in the case of the electrons the EGAMs are damped mainly by the barely trapped electrons (Fig. 8). The total EGAM growth rate (Eq. 135) and contribution of the thermal (Eq. 137) and energetic

deuterium (Eq. 139) to the mode dynamics has been calculated in the codes ORB5 and GENE in case with adiabatic electrons. The benchmark has shown 18%-consistency for the total growth rate and species contributions.

From the point of view of further possible application, the MPR diagnostic can be used, for instance, to study the energy exchange between energetic and thermal species indirectly through the zonal waves, such as EGAMs, that play a role of a mediator in this case. Other interesting effects, associated with the EGAM nonlinear evolution, are the EGAM frequency chirping, which consists in a fast modification of the mode frequency, and the saturation mechanisms. Since the frequency shift during the chirping is considered to occur as a result of the wave-particle interaction [61, 62, 63, 64, 65, 66], the MPR diagnostic can be used to investigate this phenomenon as well. The saturation mechanisms (wave-particle or wave-wave interactions) are important to investigate in order to build a theoretical model capable of predicting the saturation levels in experimentally relevant conditions, and as a consequence, the EP redistribution in phase space.

The current version of the diagnostic can be applied only to the case of mainly electrostatic modes, such as GAMs and EGAMs. As it has been discussed in Sec. 2, the reason is in the choice of the velocity space variables in ORB5. The MPR diagnostic can be extended to work with EM simulations with arbitrary  $\beta$ , by performing a proper transition from the variable  $p_{z,sp}$  to the velocity variable  $v_{\parallel,sp}$ . There are different possible areas of application of the EM-MPR diagnostic. A wider range of the modes whose dynamics is mainly controlled by wave-particle resonances, like energetic-particle driven MHD instabilities, can be investigated. For a turbulent plasma, the collisionless interactions between the EM fields and the plasma particles may lead to a secular transfer of energy from fields to particles, resulting in collisionless damping of the turbulent fluctuations. More precisely, a particular challenge in tokamak plasma and plasma physics in general is to identify the physical mechanisms by which the EM field and plasma flow fluctuations are damped and how their energy is converted to plasma heat, or some other energization of particles. For example, in astrophysical plasmas dissipation of the turbulence energy through

the Landau damping of the Alfvén waves can take place [67]. It would be interesting to investigate the influence of the plasma  $\beta$  on the energy channeling [68], especially on the contributions of different species in the plasma heating by EGAMs and Alfvén waves. There are also physical phenomena, which are specific to the space plasma, such as particle acceleration by the magnetic energy released during collisions of the magnetic islands in solar and heliospheric environments [69]. It might be interesting to investigate role of such processes in tokamak plasmas as well.

### Acknowledgement

This work has been carried out within the framework of the EUROfusion Consortium and has received funding from the Euratom research and training program 2014-2018 and 2019-2020 under grant agreement N° 633053. The views and opinions expressed herein do not necessarily reflect those of the European Commission.

Simulations, presented in this work, have been performed on the CINECA Marconi supercomputer within the framework of the OrbZONE and ORBFAST projects.

Stimulating discussions with X. Garbet and V. Grandgirard on the role of kinetic electrons in the GAM dynamics are kindly acknowledged. One of the authors, I. Novikau, would like to thank F. Vannini for useful conversations. One of the authors, A. Biancalani, also wishes to acknowledge stimulating discussions with F. Zonca and Z. Qiu on the GAM/EGAM analytical theory.

### Appendix A Derivation of the species distribution perturbations

Here, we are going to show detailed derivation of the GAM dispersion relation, based on Ref. [47, 29]. Considering a plasma consisted on deuterium and electron species ( $sp$ ), we start from a GK equation, neglecting Finite-Larmor-

Radius and Finit-Orbit-Width effects:

$$(\omega_{tr,sp}\partial_t - i(\omega - \omega_{d,sp}))\delta K_{sp} = -i\frac{F_{0,sp}Z_{sp}e}{T_{sp}}\omega\left(\tilde{\Phi} + \frac{\omega_{d,sp}}{\omega}\bar{\Phi}\right), \quad (141)$$

$$\omega_{tr,sp} = \frac{v_{\parallel,sp}}{qR_0}, \quad (142)$$

$$\omega_{d,sp} = \hat{\omega}_{d,sp}\sin\theta_p = \frac{k_r m_{sp} c}{Z_{sp} e B_0 R_0} \left( \frac{v_{\perp,sp}^2}{2} + v_{\parallel,sp}^2 \right) \sin\theta, \quad (143)$$

where  $\omega$  is a complex GAM frequency,  $\delta K_{sp}$  is a non-adiabatic perturbation of the species distribution function:

$$\delta f_{sp} = -\frac{Z_{sp}e}{T_{sp}}F_{0,sp}\tilde{\Phi} + \delta K_{sp}. \quad (144)$$

The derivative  $\partial_t$  is taken along magnetic field lines. The equilibrium distribution function  $F_{0,sp}$  is given by Eq. 79, and is normalized to 1 ( $n_{0,sp} = 1$ ). The ES potential  $\Phi$  is decomposed on the zonal (flux-surface averaged)  $\bar{\Phi}$  and non-zonal  $\tilde{\Phi}$  components. The perturbations of the species distribution functions validate the quasi-neutrality equation:

$$\langle \delta f_i \rangle = \langle \delta f_e \rangle \rightarrow \left(1 + \frac{1}{\tau_e}\right)\tilde{\Phi} = \frac{T_i}{e}(\langle \delta K_i \rangle - \langle \delta K_e \rangle), \quad (145)$$

where  $\tau_e = T_e/T_i$ , and  $\langle \cdot \rangle$  denotes the integration in velocity space. From the quasi-neutrality equation, one can derive also the vorticity equation:

$$\frac{\omega^2}{v_{A,i}^2}k_r^2\Phi = \left\langle \sum_{sp} \frac{4\pi Z_{sp}e}{c^2}\omega\omega_{d,sp}\delta K_{sp} \right\rangle, \quad (146)$$

$$v_{A,i} = \frac{B_0}{\sqrt{4\pi m_i}}. \quad (147)$$

We should introduce the ordering that will be used in the derivation of the GAM dispersion relation. Since we are dealing with GAMs, which have toroidally and mainly poloidally symmetric ES field, the ES potential perturbation is not dependent on the toroidal angle. It means, that the derivative  $\partial_t$  along magnetic field lines in the GK equation Eq. 141 becomes the derivative on the poloidal angle  $\partial_{\theta_p}$ . Moreover, the non-zonal component  $\tilde{\Phi}$ , which depends on the poloidal angle  $\theta_p$ , is considered to be much smaller than the zonal component  $\bar{\Phi}$ . Since the GAMs are sound oscillations (it means,  $\omega \sim v_{th,i}/R$ ), we

are going to use the ratio  $\omega_{d,i}/\omega \sim k_r \rho_i$  as the smallness parameter  $\epsilon$ . At the zeroth order, when the temperature is going to zero, GAM oscillations disappear  $\delta K_{sp}^{(0)} = 0$ . Apart of that, we assume, that the ratio  $\tilde{\Phi}/\bar{\Phi}$  is of the order of  $\epsilon$ . To sum up, the ordering of the system is the following one:

$$\frac{\omega_{d,i}}{\omega} \sim \mathcal{O}(\epsilon), \quad (148)$$

$$\Phi = \Phi^{(0)} + \Phi^{(1)}, \quad (149)$$

$$\Phi^{(0)} = \bar{\Phi} \sim \mathcal{O}(1), \quad \Phi^{(1)} = \tilde{\Phi} \sim \mathcal{O}(\epsilon), \quad (150)$$

$$\delta K_{sp} = \delta K_{sp}^{(0)} + \delta K_{sp}^{(1)}, \quad (151)$$

$$\delta K_{sp}^{(0)} = 0. \quad (152)$$

Now, we are going to consider the GK equation separately for different species. We start from the case of electrons. Due to their small mass, the electrons have a high speed along the magnetic field, leading to the domination of the transit frequency on all other frequencies:

$$\frac{\omega_{tr,e}}{\omega} \sim \mathcal{O}(\epsilon^{-1}). \quad (153)$$

On the other hand, the ordering of the drift frequency is the same for all species, since it does not depend on the species mass. We expand the GK equation Eq. 141 up to the  $\mathcal{O}(\epsilon)$  order:

$$\left( \frac{\omega_{tr,e}}{\omega} \partial_{\theta_p} - i \right) \delta K_e^{(1)} = i \frac{F_{0,e} e}{T_e} \left( \tilde{\Phi} + \frac{\omega_{d,e}}{\omega} \bar{\Phi} \right). \quad (154)$$

By taking the flux-averaging (in this case, averaging on the poloidal angle) of the equation, one gets  $\overline{\delta K_e} = 0$ . By considering only the terms of the  $\mathcal{O}(1)$  order in Eq. 154, one obtains that  $\widetilde{\delta K_e}^{(1)} = 0$ . It means that we are dealing with adiabatic electrons, whose distribution perturbation function does not have any kinetic part:

$$\delta K_e = 0. \quad (155)$$

Now, we are going to work with the ion GK equation. It is known that the ion transit frequency  $\omega_{tr,i}$  is of the order of the sound frequency, it means, it is

of the order of the GAM frequency:

$$\frac{\omega_{tr,i}}{\omega} \sim \mathcal{O}(1). \quad (156)$$

As a result, considering only the terms up to  $\mathcal{O}(\epsilon)$ , we get for the ions that

$$\left(\frac{\omega_{tr,i}}{\omega}\partial_{\theta_p} - i\right)\delta K_i^{(1)} = -i\frac{F_{0,i}e}{T_i}\left(\tilde{\Phi} + \frac{\omega_{d,i}}{\omega}\bar{\Phi}\right). \quad (157)$$

From the flux-surface averaging, one gets again that  $\overline{\delta K_i} = 0$ . Now, we are splitting the distribution and field perturbations on zonal,  $\cos\theta_p$  and  $\sin\theta_p$  components:

$$\Phi = \bar{\Phi} + \tilde{\Phi}_c \cos\theta_p + \tilde{\Phi}_s \sin\theta_p, \quad (158)$$

$$\delta K_i = \overline{\delta K_i}^{(1)} (= 0) + \widetilde{\delta K_{i,c}}^{(1)} \cos\theta_p + \widetilde{\delta K_{i,s}}^{(1)} \sin\theta_p. \quad (159)$$

Considering separately zonal terms and terms in front of  $\cos\theta$  and  $\sin\theta$  functions, one gets the following system of equations:

$$\begin{pmatrix} -i\omega & 0 & \omega_{tr,i} \\ 0 & -i\omega & 0 \\ -\omega_{tr,i} & 0 & -i\omega \end{pmatrix} \begin{pmatrix} \widetilde{\delta K_{i,c}}^{(1)} \\ \widetilde{\delta K_i}^{(1)} \\ \widetilde{\delta K_{i,s}}^{(1)} \end{pmatrix} = -\frac{iF_{0,i}e\omega}{T_i} \begin{pmatrix} 1 & 0 & 0 \\ 0 & 0 & 0 \\ 0 & \hat{\omega}_{d,i}/\omega & 1 \end{pmatrix} \begin{pmatrix} \tilde{\Phi}_c \\ \bar{\Phi} \\ \tilde{\Phi}_s \end{pmatrix}. \quad (160)$$

From this system one can find the kinetic part of the distribution perturbation for the ions:

$$\widetilde{\delta K_{i,c}}^{(1)} = \frac{-iF_{0,i}e\omega}{T_i(\omega^2 - \omega_{tr,i}^2)} \left( i\omega\tilde{\Phi}_c + \omega_{tr,i}\tilde{\Phi}_s + \omega_{tr,i}\frac{\hat{\omega}_{d,i}}{\omega}\bar{\Phi} \right), \quad (161)$$

$$\widetilde{\delta K_{i,s}}^{(1)} = \frac{-iF_{0,i}e\omega}{T_i(\omega^2 - \omega_{tr,i}^2)} \left( -\omega_{tr,i}\tilde{\Phi}_c + i\omega\tilde{\Phi}_s + i\hat{\omega}_{d,i}\bar{\Phi} \right). \quad (162)$$

After that, by putting Eq. 161 and Eq. 162 into the quasi-neutrality equation Eq. 145, and taking into account the adiabaticity of electrons (Eq. 155), one can find expressions for the non-zonal components  $\tilde{\Phi}_c$  and  $\tilde{\Phi}_s$  of the ES potential:

$$\begin{aligned} & \left(1 + \frac{1}{\tau_e}\right) (\bar{\Phi} + \tilde{\Phi}_c \cos\theta + \tilde{\Phi}_s \sin\theta) = \\ & \frac{T_i}{e} \left( \left\langle \widetilde{\delta K_{i,c}}^{(1)} \right\rangle \cos\theta_p + \left\langle \widetilde{\delta K_{i,s}}^{(1)} \right\rangle \sin\theta_p \right). \end{aligned} \quad (163)$$

First of all, one should notice that  $F_{0,i}$  (Eq. 79) and  $\hat{\omega}_{d,i}$  (Eq. 143) are even functions of the parallel speed  $v_{\parallel,i}$ , and  $\omega_{tr,i}$  is an odd one. Because of that, the terms proportional to  $\omega_{tr,i}$  in Eq. 161 and Eq. 162 will disappear after the velocity integration  $\langle \cdot \rangle$ . During the velocity integration, we are going to use an expression of the Plasma Dispersion Function (PDF) [70]:

$$\mathcal{Z}(z) = \frac{1}{\sqrt{\pi}} \int_{-\infty}^{+\infty} \frac{\exp(-y^2)}{y-z} dy = -\sqrt{\pi} \exp(-z^2) (\text{erfi}(z) + i), \quad (164)$$

where  $\text{Im}(z) < 0$ ,  $\text{erfi}(z)$  is the Imaginary Error Function, and the following integrals can be evaluated using the PDF:

$$\frac{1}{\sqrt{\pi}} \int_{-\infty}^{+\infty} \frac{\exp(-y^2)}{y^2 - z^2} dy = \frac{\mathcal{Z}(z)}{z}, \quad (165)$$

$$\frac{1}{\sqrt{\pi}} \int_{-\infty}^{+\infty} \frac{y^2 \exp(-y^2)}{y^2 - z^2} dy = 1 + z\mathcal{Z}(z), \quad (166)$$

$$\frac{1}{\sqrt{\pi}} \int_{-\infty}^{+\infty} \frac{y^4 \exp(-y^2)}{y^2 - z^2} dy = \frac{1}{2} + z^2 + z^3\mathcal{Z}(z). \quad (167)$$

We start from the first term on the right hand side in Eq. 163:

$$\left\langle \widetilde{\delta K}_{i,c}^{(1)} \right\rangle = -\frac{e\omega^2 \widetilde{\Phi}_c}{T_i v_{th,i}^3 \pi^{3/2}} \left\langle \frac{\exp\left(-\frac{v_{\parallel,i}^2 + v_{\perp,i}^2}{v_{th,i}^2}\right)}{\omega_{tr,i}^2 - \omega^2} \right\rangle, \quad (168)$$

where  $v_{th,i} = \sqrt{2T_i/m_i}$ . Integration in the velocity space is performed in cylindrical coordinates:

$$\int_{-\infty}^{+\infty} d^3v = 2\pi \int_0^{+\infty} v_{\perp} dv_{\perp} \int_{-\infty}^{+\infty} dv_{\parallel}. \quad (169)$$

Since that, we have

$$\left\langle \frac{\exp\left(-\frac{v_{\parallel,i}^2 + v_{\perp,i}^2}{v_{th,i}^2}\right)}{\omega_{tr,i}^2 - \omega^2} \right\rangle = 2\pi \frac{T_i}{m_i} \int_{-\infty}^{+\infty} \frac{\exp(-v_{\parallel}^2/v_{th,i}^2)}{\omega_{tr,i}^2 - \omega^2} dv_{\parallel}. \quad (170)$$

By performing the following change of variables

$$y = \frac{v_{\parallel}}{v_{th,i}}, \quad z = \frac{\omega}{\omega_{0,i}}, \quad \omega_{0,i} = \frac{v_{th,i}}{qR_0}, \quad (171)$$

one gets an integral, similar to Eq. 165:

$$\int_{-\infty}^{+\infty} \frac{\exp(-v_{\parallel}^2/v_{th,i}^2)}{\omega_{tr,i}^2 - \omega^2} dv_{\parallel} = \frac{\sqrt{\pi}(qR_0)^2}{v_{th,i}} \frac{1}{\sqrt{\pi}} \int_{-\infty}^{+\infty} \frac{\exp(-y^2)}{y^2 - z^2} dy. \quad (172)$$

Combining Eq. 165, 172 and 170, and putting the result into Eq. 168, one finally gets

$$\langle \delta \widetilde{K}_{i,c}^{(1)} \rangle = -\frac{e\widetilde{\Phi}_c}{T_i} z \mathcal{Z}(z). \quad (173)$$

Now, we are going to consider the second term on the right hand side of Eq. 163:

$$\left\langle \delta \widetilde{K}_{i,s}^{(1)} \right\rangle = -\frac{e\omega^2}{T_i} \left\langle \frac{F_{0,i}}{\omega_{tr,i}^2 - \omega^2} \right\rangle \widetilde{\Phi}_s - \frac{e\omega}{T_i} \left\langle \frac{F_{0,i} \hat{\omega}_{d,i}}{\omega_{tr,i}^2 - \omega^2} \right\rangle \overline{\Phi}. \quad (174)$$

The first term is evaluated in the same way as it has been done above:

$$-\frac{e\omega^2}{T_i} \left\langle \frac{F_{0,i}}{\omega_{tr,i}^2 - \omega^2} \right\rangle \widetilde{\Phi}_s = -\frac{e\widetilde{\Phi}_s}{T_i} z \mathcal{Z}(z). \quad (175)$$

The velocity integral in the second term is

$$\left\langle \frac{F_{0,i} \hat{\omega}_{d,i}}{\omega_{tr,i}^2 - \omega^2} \right\rangle = \pi v_{th,i}^2 \int_{-\infty}^{+\infty} dv_{\parallel} \frac{\left( v_{th,i}^2/2 + v_{\parallel}^2 \right) \exp\left(-v_{\parallel}^2/v_{th,i}^2\right)}{\omega_{tr,i}^2 - \omega^2}, \quad (176)$$

where we have already performed integration on the perpendicular velocity. The first part of this integral can be found by using again Eq. 165:

$$\pi \frac{v_{th,i}^4}{2} \int_{-\infty}^{+\infty} dv_{\parallel} \frac{\exp\left(-v_{\parallel}^2/v_{th,i}^2\right)}{\omega_{tr,i}^2 - \omega^2} = \frac{\pi^{3/2} v_{th,i}^3 (qR_0)^2}{2z} \mathcal{Z}(z). \quad (177)$$

The second part of the integral Eq. 176, using Eq. 166, is evaluated to

$$\pi v_{th,i}^2 \int_{-\infty}^{+\infty} dv_{\parallel} \frac{v_{\parallel}^2 \exp\left(-v_{\parallel}^2/v_{th,i}^2\right)}{\omega_{tr,i}^2 - \omega^2} = -\pi^{3/2} v_{th,i}^3 (qR_0)^2 (1 + z \mathcal{Z}(z)). \quad (178)$$

By using Eq. 175, 177 and 178, one can finally evaluate the second term on the right hand side in Eq. 163,

$$\left\langle \delta \widetilde{K}_{i,s}^{(1)} \right\rangle = \frac{e}{T_i} \left( -z \mathcal{Z}(z) \widetilde{\Phi}_s - \frac{2k_r c T_i}{e B_0 R_0 \omega_{0,i}} N(z) \overline{\Phi} \right), \quad (179)$$

$$\omega_{0,i} = \frac{v_{th,i}}{qR_0}, \quad (180)$$

$$N(z) = z + \left( \frac{1}{2} + z^2 \right) \mathcal{Z}(z), \quad (181)$$

where we have introduced a function  $N(z)$  (to compare to Eq. 71).

Now, by putting Eq. 173 and Eq. 179 into Eq. 163, and considering separately terms in front of  $\cos\theta_p$  and  $\sin\theta_p$ , we can find expressions for the non-zonal components of the ES potential:

$$\tilde{\Phi}_c = 0, \quad (182)$$

$$\tilde{\Phi}_s = -\frac{2k_r c T_i}{e B_0 R_0} \frac{1}{\omega} \frac{N(z)}{D(z)} \bar{\Phi}, \quad (183)$$

$$D(z) = \frac{1}{z} \left( 1 + \frac{1}{\tau_e} \right) + \mathcal{Z}(z), \quad (184)$$

where a function  $D(z)$  has been introduced (to compare to Eq. 72).

Now, we are interested only in the kinetic part of the species distribution function, that should be used in the power exchange expression Eq. 57. In Eq. 57 one performs an integration in space, including the integration along the poloidal direction. In case of the GAM dynamics,  $\dot{\mathbf{R}}_0 \cdot \mathbf{E} \sim \sin\theta_p$ , as one can see in Eq. 85. Because of that, terms in  $\delta\widetilde{K}$ , that are proportional to  $\cos\theta_p$ , will not contribute to the power exchange. It means, we need to consider only the term  $\delta\widetilde{K}_{i,s}^{(1)}$ . To sum up, for the power exchange signal, we consider the following distribution function:

$$\delta f = \delta\widetilde{K}_{i,s}^{(1)} \sin\theta_p. \quad (185)$$

By putting results from Eq. 182 and Eq. 183 to Eq. 162, one can obtain a final expression for the distribution perturbation, shown in Eq. 78.

Finally, it should be noticed, that using a flux-surface-averaged vorticity equation, derived from Eq. 146:

$$\frac{\omega^2}{v_{A,i}^2} k_r^2 \bar{\Phi} = \left\langle \frac{2\pi e}{c^2} \omega \hat{\omega}_{d,i} \delta\widetilde{K}_{i,s}^{(1)} \right\rangle, \quad (186)$$

and the integral Eq. 167, one can get the GAM dispersion relation Eq. 70.

## Appendix B Evaluation of the Plasma Dispersion Function

The Plasma Dispersion Function (PDF)

$$\mathcal{Z}(z) = \frac{1}{\sqrt{\pi}} \int_{-\infty}^{+\infty} \frac{\exp(-t^2)}{t-z} dt \quad (187)$$

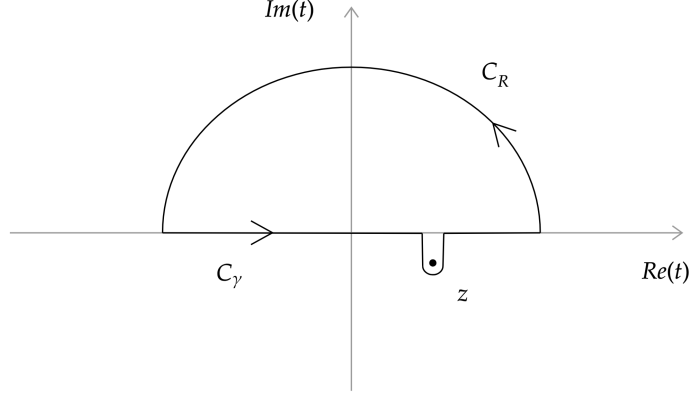


Figure 11: Domain of integration of the Plasma Dispersion Function. The contour  $C_\gamma$  is curved in such a way to keep the pole  $z$  on the left hand side. After that, we assume that the pole falls on the contour  $C_\gamma$  from the domain surrounded by a closed contour  $\Gamma = C_\gamma + C_R$ .

is defined for the case of  $Im(z) > 0$ . But since we are dealing with the Landau damping, we have to extend analytically this integral to the case of  $Im(z) < 0$ . The analytical continuation is there carried out in such a way that the path of integration is deformed into a contour for which the pole  $z$  is always sitting on the left hand side. Now, we can consider a closed contour  $\Gamma = C_\gamma + C_R$ , as it is shown in Fig. 11, where  $C_\gamma$  goes along a real axis and is curved near the pole  $z$  to keep it on the left hand side, and  $C_R$  is a half circle with a radius  $R \rightarrow +\infty$ . By denoting the integrand of the PDF as  $G(t, z)$

$$G(t, z) = \frac{1}{\sqrt{\pi}} \frac{\exp(-t^2)}{t - z}, \quad (188)$$

we have the following equality:

$$\int_{\Gamma} G(t, z) dt = \int_{C_\gamma} G(t, z) dt + \int_{C_R} G(t, z) dt. \quad (189)$$

Since

$$\lim_{R \rightarrow +\infty} \int_{C_R} G(t, z) dt = 0, \quad (190)$$

the second integral on the right hand side of Eq. 189 is equal to 0. The integral along the  $C_\gamma$  in the limit of a big radius  $R$  represents the analytical continuation

of PDF. If we assume, that the pole  $z$  is sitting on the curved contour, in this case, we can evaluate PDF using the principle value integral, more precisely, by applying the Sokhotski - Plemelj theorem:

$$\int_{\Gamma} G(t, z) dt = \int_{C_{\gamma}} G(t, z) dt = P.V. \int_{C_{\gamma}} G(t, z) dt - i\sqrt{\pi} \exp(-z^2). \quad (191)$$

Now, for the sake of numerical calculations, we would like to relate the principle value integral to the Imaginary Error Function  $Erfi(z)$ . It is known that the Hilbert transform of the Gaussian can be related to  $Erfi(z)$  (Ref. [71]) as

$$\frac{1}{\sqrt{\pi}} P.V. \int_{-\infty}^{+\infty} \frac{\exp(-t^2)}{t - z} dt = -\sqrt{\pi} \exp(-z^2) Erfi(z). \quad (192)$$

Finally, the Plasma Dispersion Function  $\mathcal{Z}(z)$ , analytically extended to the lower half of the imaginary plane, can be expressed using the following equation:

$$\mathcal{Z}(z) = -\sqrt{\pi} \exp(-z^2)(i + Erfi(z)). \quad (193)$$

## Appendix C EM simulation with a smaller plasma beta

The EGAM damping on the passing electrons that is observed in Eq. 114, must be a numerical phenomenon, which occurs due to the  $A_{\parallel}$  contribution to the velocity coordinate Eq. 59. Since  $A_{\parallel}$  reduces with plasma  $\beta$ , exactly the same EM simulation as in Sec. 5 has been launched, but with a smaller  $\beta = 2.7 \cdot 10^{-5}$  (smaller electron density). In Sec. 5 the simulation has been performed with  $\beta = 2.7 \cdot 10^{-4}$ . The result EGAM growth and damping rates in this case are

$$total : \quad \gamma[\sqrt{2}v_{th,i}/R_0] = 8.7 \cdot 10^{-2} \pm 3.3 \cdot 10^{-3}, \quad (194)$$

$$thermal\ deuterium : \quad \gamma[\sqrt{2}v_{th,i}/R_0] = -3.95 \cdot 10^{-1} \pm 3.9 \cdot 10^{-3}, \quad (195)$$

$$thermal\ electrons : \quad \gamma[\sqrt{2}v_{th,i}/R_0] = -2.1 \cdot 10^{-2} \pm 1.2 \cdot 10^{-3}, \quad (196)$$

$$fast\ deuterium : \quad \gamma[\sqrt{2}v_{th,i}/R_0] = 5.02 \cdot 10^{-1} \pm 4.0 \cdot 10^{-3}, \quad (197)$$

that should be compared with Eq. 105 and Eqs. 108-110 respectively. One can see that only the electron component has been changed. Finally, integrating the

energy transfer signal in the same velocity domains as in Fig. 8b, we obtain

$$e1 : \quad \gamma[\sqrt{2}v_{th,i}/R_0] = -1.36 \cdot 10^{-2} \pm 5.1 \cdot 10^{-4}, \quad (198)$$

$$e2 : \quad \gamma[\sqrt{2}v_{th,i}/R_0] = 2.1 \cdot 10^{-3} \pm 1.4 \cdot 10^{-4}, \quad (199)$$

$$e3 : \quad \gamma[\sqrt{2}v_{th,i}/R_0] = -8.3 \cdot 10^{-3} \pm 8.7 \cdot 10^{-4}. \quad (200)$$

Corresponding field-electron energy transfer signals in velocity space are shown in Fig. 12. Since the EGAM linear dynamics must be mostly electrostatic, its dynamics should not depend on the value of plasma  $\beta$  (plasma density). Because of that, corresponding damping and growth rates should remain the same. More precisely, the component of the barely trapped electrons ( $e1$ ) remains the same as in Eq. 112. On the other hand, the contribution of the passing electrons ( $e3$ ) has decreased in comparison to Eq. 114, which indicates its dependence on the magnetic potential, as it is supposed to be in the  $p_{\parallel}$ -formulation.

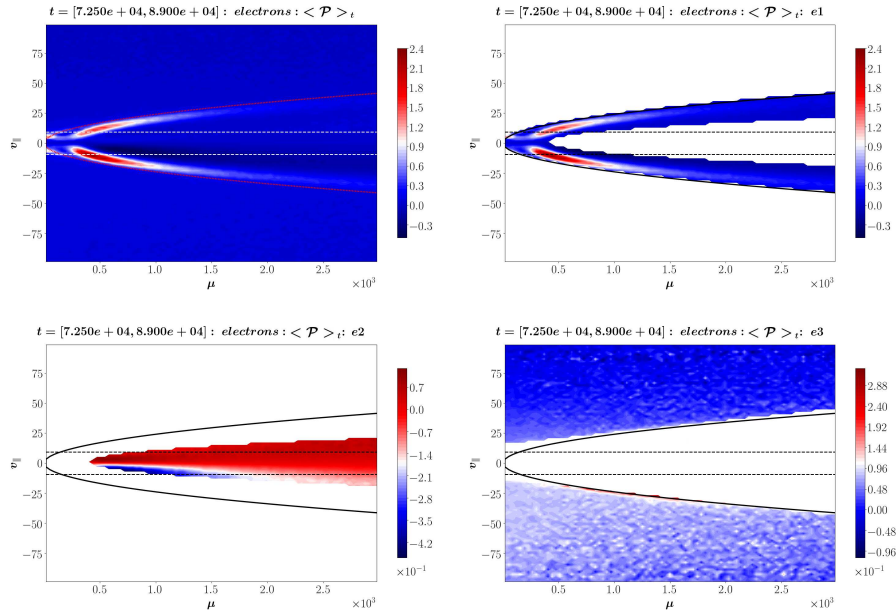


Figure 12: Energy transfer signal between the zonal radial electric field and electrons in the whole velocity domain (upper left plot), as well as in the domains of barely trapped electrons  $e1$  (upper right), deeply trapped electrons  $e2$  (lower left), passing electrons  $e3$  (lower right). Note different scales in the colorbars.

## References

- [1] A. J. Brizard, T. S. Hahm, Foundations of nonlinear gyrokinetic theory, *Rev. Mod. Phys.* 79 (2007) 421–468 (Apr 2007). doi:10.1103/RevModPhys.79.421.  
URL <https://link.aps.org/doi/10.1103/RevModPhys.79.421>
- [2] R. Hatzky, A. Koenies, A. Mishchenko, Electromagnetic gyrokinetic pic simulation with an adjustable control variates method, *Journal of Computational Physics* 225 (1) (2007) 568 – 590 (2007). doi:<https://doi.org/10.1016/j.jcp.2006.12.019>.  
URL <http://www.sciencedirect.com/science/article/pii/S0021999106006085>

- [3] A. Mishchenko, A. Bottino, R. Hatzky, E. Sonnendruecker, R. Kleiber, A. Koenies, Mitigation of the cancellation problem in the gyrokinetic particle-in-cell simulations of global electromagnetic modes, *Physics of Plasmas* 24 (8) (2017) 081206 (2017). arXiv:<https://doi.org/10.1063/1.4997540>, doi:10.1063/1.4997540.  
URL <https://doi.org/10.1063/1.4997540>
- [4] N. Winsor, J. L. Johnson, J. M. Dawson, Geodesic acoustic waves in hydromagnetic systems, *The Physics of Fluids* 11 (11) (1968) 2448–2450 (1968). arXiv:<https://aip.scitation.org/doi/pdf/10.1063/1.1691835>, doi:10.1063/1.1691835.  
URL <https://aip.scitation.org/doi/abs/10.1063/1.1691835>
- [5] P. H. Diamond, S.-I. Itoh, K. Itoh, T. S. Hahm, Zonal flows in plasma—a review, *Plasma Physics and Controlled Fusion* 47 (5) (2005) R35–R161 (apr 2005). doi:10.1088/0741-3335/47/5/r01.  
URL <https://doi.org/10.1088/0741-3335/47/5/r01>
- [6] Z. Qiu, L. Chen, F. Zonca, Kinetic theory of geodesic acoustic modes in toroidal plasmas: a brief review, *Plasma Science and Technology* 20 (9) (2018) 094004 (jul 2018). doi:10.1088/2058-6272/aab4f0.  
URL <https://doi.org/10.1088/2058-6272/aab4f0>
- [7] C. Boswell, H. Berk, D. Borba, T. Johnson, S. Pinches, S. Sharapov, Observation and explanation of the jet  $n=0$  chirping mode, *Physics Letters A* 358 (2) (2006) 154 – 158 (2006). doi:<https://doi.org/10.1016/j.physleta.2006.05.030>.  
URL <http://www.sciencedirect.com/science/article/pii/S0375960106007031>
- [8] G. Y. Fu, Energetic-particle-induced geodesic acoustic mode, *Phys. Rev. Lett.* 101 (2008) 185002 (Oct 2008). doi:10.1103/PhysRevLett.101.185002.  
URL <https://link.aps.org/doi/10.1103/PhysRevLett.101.185002>

- [9] L. Horváth, G. Papp, P. Lauber, G. Por, A. Gude, V. Igochine, B. Geiger, M. Maraschek, L. Guimaraes, V. Nikolaeva, G. Pokol, The ASDEX Upgrade Team, Experimental investigation of the radial structure of energetic particle driven modes, *Nuclear Fusion* 56 (11) (2016) 112003 (jul 2016). doi:10.1088/0029-5515/56/11/112003.  
URL <https://doi.org/10.1088/0029-5515/56/11/112003>
- [10] T. Ido, Abrupt excitation of energetic-particle-driven geodesic acoustic mode in the large helical device, *AIP Conference Proceedings* 1993 (1) (2018) 020002 (2018). arXiv:<https://aip.scitation.org/doi/pdf/10.1063/1.5048712>, doi:10.1063/1.5048712.  
URL <https://aip.scitation.org/doi/abs/10.1063/1.5048712>
- [11] G. G. Howes, K. G. Klein, T. C. Li, Diagnosing collisionless energy transfer using fieldparticle correlations: Vlasovpoisson plasmas, *Journal of Plasma Physics* 83 (1) (2017) 705830102 (2017). doi:10.1017/S0022377816001197.
- [12] A. Keiling, *Alfvén Waves and Their Roles in the Dynamics of the Earth's Magnetotail: A Review*, Vol. 142, Springer Netherlands, 2009 (2009). doi:10.1007/s11214-008-9463-8.
- [13] S. Jolliet, A. Bottino, P. Angelino, R. Hatzky, T. Tran, B. Mcmillan, O. Sauter, K. Appert, Y. Idomura, L. Villard, A global collisionless pic code in magnetic coordinates, *Computer Physics Communications* 177 (5) (2007) 409 – 425 (2007). doi:<https://doi.org/10.1016/j.cpc.2007.04.006>.  
URL <http://www.sciencedirect.com/science/article/pii/S0010465507002251>
- [14] A. Bottino, E. Sonnendruecker, Monte carlo particle-in-cell methods for the simulation of the vlasovmaxwell gyrokinetic equations, *Journal of Plasma Physics* 81 (5) (2015) 435810501 (2015). doi:10.1017/S0022377815000574.

- [15] R. Hatzky, T. M. Tran, A. Könies, R. Kleiber, S. J. Allfrey, Energy conservation in a nonlinear gyrokinetic particle-in-cell code for ion-temperature-gradient-driven modes in  $\theta$ -pinch geometry, *Phys. Plasmas* 9 (2002) 898–912 (Mar. 2002). doi:10.1063/1.1449889.
- [16] A. Bottino, A. G. Peeters, O. Sauter, J. Vaclavik, L. Villard, Simulations of global electrostatic microinstabilities in asdex upgrade discharges, *Physics of Plasmas* 11 (1) (2004) 198–206 (2004). arXiv:<https://doi.org/10.1063/1.1633554>, doi:10.1063/1.1633554. URL <https://doi.org/10.1063/1.1633554>
- [17] N. Tronko, A. Bottino, E. Sonnendruecker, Second order gyrokinetic theory for particle-in-cell codes, *Physics of Plasmas* 23 (8) (2016) 082505 (2016). arXiv:<https://doi.org/10.1063/1.4960039>, doi:10.1063/1.4960039. URL <https://doi.org/10.1063/1.4960039>
- [18] T. Ido, M. Osakabe, A. Shimizu, T. Watari, M. Nishiura, K. Toi, K. Ogawa, K. Itoh, I. Yamada, R. Yasuhara, Y. Yoshimura, S. K. and, Identification of the energetic-particle driven GAM in the LHD, *Nuclear Fusion* 55 (8) (2015) 083024 (jul 2015). doi:10.1088/0029-5515/55/8/083024. URL <https://doi.org/10.1088/0029-5515/55/8/083024>
- [19] M. Osakabe, T. Ido, K. Ogawa, A. Shimizu, M. Yokoyama, R. Seki, C. Suzuki, M. Isobe, K. Toi, D. A. Spong, K. Nagaoka, Y. Takeiri, H. Igami, T. Seki, K. Nagasaki, LHD experiment group, Indication of bulk-ion heating by energetic particle driven geodesic acoustic modes on lhd, in: 25th IAEA fusion energy conference, 2014 (2014). URL [https://inis.iaea.org/search/search.aspx?orig\\_q=RN:47070985](https://inis.iaea.org/search/search.aspx?orig_q=RN:47070985)
- [20] H. S. Zhang, Z. Lin, Trapped electron damping of geodesic acoustic mode, *Physics of Plasmas* 17 (7) (2010) 072502 (2010). arXiv:<https://doi.org/10.1063/1.3447879>, doi:10.1063/1.3447879. URL <https://doi.org/10.1063/1.3447879>

- [21] A. Biancalani, A. Bottino, C. Ehrlacher, V. Grandgirard, G. Merlo, I. Novikau, Z. Qiu, E. Sonnendruecker, X. Garbet, T. Goerler, S. Leerink, F. Palermo, D. Zarzoso, Cross-code gyrokinetic verification and benchmark on the linear collisionless dynamics of the geodesic acoustic mode, *Physics of Plasmas* 24 (6) (2017) 062512 (2017). [arXiv:https://doi.org/10.1063/1.4985571](https://arxiv.org/abs/10.1063/1.4985571), [doi:10.1063/1.4985571](https://doi.org/10.1063/1.4985571).  
URL <https://doi.org/10.1063/1.4985571>
- [22] I. Novikau, A. Biancalani, A. Bottino, G. D. Conway, O. D. Gürçan, P. Manz, P. Morel, E. Poli, A. Di Siena, Linear gyrokinetic investigation of the geodesic acoustic modes in realistic tokamak configurations, *Physics of Plasmas* 24 (12) (2017) 122117 (2017). [arXiv:https://doi.org/10.1063/1.5003784](https://arxiv.org/abs/10.1063/1.5003784), [doi:10.1063/1.5003784](https://doi.org/10.1063/1.5003784).  
URL <https://doi.org/10.1063/1.5003784>
- [23] C. Ehrlacher, X. Garbet, V. Grandgirard, Y. Sarazin, P. Donnel, E. Caschera, P. Ghendrih, D. Zarzoso, Contribution of kinetic electrons to GAM damping, *Journal of Physics: Conference Series* 1125 (2018) 012010 (nov 2018). [doi:10.1088/1742-6596/1125/1/012010](https://doi.org/10.1088/1742-6596/1125/1/012010).  
URL <https://doi.org/10.1088/1742-6596/1125/1/012010>
- [24] M. N. Rosenbluth, F. L. Hinton, Poloidal flow driven by ion-temperature-gradient turbulence in tokamaks, *Phys. Rev. Lett.* 80 (1998) 724–727 (Jan 1998). [doi:10.1103/PhysRevLett.80.724](https://doi.org/10.1103/PhysRevLett.80.724).  
URL <https://link.aps.org/doi/10.1103/PhysRevLett.80.724>
- [25] P. Manz, G. S. Xu, B. N. Wan, H. Q. Wang, H. Y. Guo, I. Cziegler, N. Fedorczak, C. Holland, S. H. Mueller, S. C. Thakur, M. Xu, K. Miki, P. H. Diamond, G. R. Tynan, Zonal flow triggers the l-h transition in the experimental advanced superconducting tokamak, *Physics of Plasmas* 19 (7) (2012) 072311 (2012). [arXiv:https://doi.org/10.1063/1.4737612](https://arxiv.org/abs/10.1063/1.4737612), [doi:10.1063/1.4737612](https://doi.org/10.1063/1.4737612).  
URL <https://doi.org/10.1063/1.4737612>

- [26] L. Schmitz, L. Zeng, T. L. Rhodes, J. C. Hillesheim, E. J. Doyle, R. J. Groebner, W. A. Peebles, K. H. Burrell, G. Wang, Role of zonal flow predator-prey oscillations in triggering the transition to h-mode confinement, *Phys. Rev. Lett.* 108 (2012) 155002 (Apr 2012). doi:10.1103/PhysRevLett.108.155002.  
URL <https://link.aps.org/doi/10.1103/PhysRevLett.108.155002>
- [27] L. Chen, Z. Lin, R. White, Excitation of zonal flow by drift waves in toroidal plasmas, *Physics of Plasmas* 7 (8) (2000) 3129–3132 (2000). arXiv:<https://doi.org/10.1063/1.874222>, doi:10.1063/1.874222.  
URL <https://doi.org/10.1063/1.874222>
- [28] A. Medvedeva, C. Bottureau, F. Clairet, P. Hennequin, U. Stroth, G. Birkenmeier, M. Cavedon, G. D. Conway, T. Happel, S. Heuraux, D. Molina, A. Silva, M. W. and, Density profile and turbulence evolution during l-h transition studied with the ultra-fast swept reflectometer on ASDEX upgrade, *Plasma Physics and Controlled Fusion* 59 (12) (2017) 125014 (nov 2017). doi:10.1088/1361-6587/aa9251.  
URL <https://doi.org/10.1088/1361-6587/aa9251>
- [29] F. Zonca, L. Chen, Radial structures and nonlinear excitation of geodesic acoustic modes, *EPL (Europhysics Letters)* 83 (3) (2008) 35001 (jul 2008). doi:10.1209/0295-5075/83/35001.  
URL <https://doi.org/10.1209/0295-5075/83/35001>
- [30] G. D. Conway, C. Angioni, F. Ryter, P. Sauter, J. Vicente, Mean and oscillating plasma flows and turbulence interactions across the  $l-h$  confinement transition, *Phys. Rev. Lett.* 106 (2011) 065001 (Feb 2011). doi:10.1103/PhysRevLett.106.065001.  
URL <https://link.aps.org/doi/10.1103/PhysRevLett.106.065001>
- [31] T. Kobayashi, M. Sasaki, T. Ido, K. Kamiya, Y. Miura, Y. Nagashima, K. Ida, S. Inagaki, A. Fujisawa, S.-I. Itoh, K. Itoh, Quantification of turbulent driving forces for the geodesic acoustic mode in the jft-2m toka-

mak, Phys. Rev. Lett. 120 (2018) 045002 (Jan 2018). doi:10.1103/PhysRevLett.120.045002.

URL <https://link.aps.org/doi/10.1103/PhysRevLett.120.045002>

- [32] A. S. Liang, W. L. Zhong, X. L. Zou, X. R. Duan, Z. C. Yang, J. Wen, G. L. Xiao, M. Jiang, Z. B. Shi, P. W. Shi, W. Chen, X. M. Song, D. L. Yu, L. W. Yan, Y. Liu, Q. W. Yang, J. Q. Dong, X. T. Ding, M. Xu, Pedestal dynamics across low to high confinement regime in the hl-2a tokamak, Physics of Plasmas 25 (2) (2018) 022501 (2018). arXiv:<https://doi.org/10.1063/1.5013074>, doi:10.1063/1.5013074.

URL <https://doi.org/10.1063/1.5013074>

- [33] B. Scott, The geodesic transfer effect on zonal flows in tokamak edge turbulence, Physics Letters A 320 (1) (2003) 53 – 62 (2003). doi:<https://doi.org/10.1016/j.physleta.2003.10.080>.

URL <http://www.sciencedirect.com/science/article/pii/S037596010301644X>

- [34] C. Silva, R. Henriques, C. Hidalgo, H. Fernandes, Experimental evidence of turbulence regulation by time-varying exb flows, Nuclear Fusion 58 (2) (2017) 026017 (dec 2017). doi:10.1088/1741-4326/aa9dc0.

URL <https://doi.org/10.1088/1741-4326/aa9dc0>

- [35] D. Zarzoso, Y. Sarazin, X. Garbet, R. Dumont, A. Strugarek, J. Abiteboul, T. Cartier-Michaud, G. Dif-Pradalier, P. Ghendrih, V. Grandgirard, G. Latu, C. Passeron, O. Thomine, Impact of energetic-particle-driven geodesic acoustic modes on turbulence, Phys. Rev. Lett. 110 (2013) 125002 (Mar 2013). doi:10.1103/PhysRevLett.110.125002.

URL <https://link.aps.org/doi/10.1103/PhysRevLett.110.125002>

- [36] D. Zarzoso, P. Migliano, V. Grandgirard, G. Latu, C. Passeron, Nonlinear interaction between energetic particles and turbulence in gyro-kinetic simulations and impact on turbulence properties, Nuclear Fusion 57 (7) (2017)

072011 (jun 2017). doi:10.1088/1741-4326/aa7351.

URL <https://doi.org/10.1088/1741-4326/aa7351>

- [37] M. Sasaki, N. Kasuya, K. Itoh, Y. Kosuga, M. Lesur, K. Hallatschek, S.-I. Itoh, Toroidal momentum channeling of geodesic acoustic modes driven by fast ions, *Nuclear Fusion* 57 (3) (2017) 036025 (jan 2017). doi:10.1088/1741-4326/aa4eb4.

URL <https://doi.org/10.1088/1741-4326/aa4eb4>

- [38] M. Sasaki, K. Itoh, K. Hallatschek, N. Kasuya, M. Lesur, Y. Kosuga, S.-I. Itoh, Enhancement and suppression of turbulence by energetic-particle-driven geodesic acoustic modes, *Scientific Reports* 7 (2017) 16767 (2017). doi:10.1038/s41598-017-17011-y.

URL <https://doi.org/10.1038/s41598-017-17011-y>

- [39] A. Biancalani, A. Bottino, N. Carlevaro, A. Di Siena, T. Görler, G. Montani, I. Novikau, D. Zarzoso, Nonlinear gyrokinetic investigation of energetic particle driven geodesic acoustic modes, in: 45th EPS Conference on Plasma Physics, P2.1003, Prague, Czech Republic, 2018 (2-6 July 2018).

- [40] N. Tronko, C. Chandre, Second-order nonlinear gyrokinetic theory: from the particle to the gyrocentre, *Journal of Plasma Physics* 84 (3) (2018) 925840301 (2018). doi:10.1017/S0022377818000430.

- [41] A. Biancalani, A. Bottino, P. Lauber, D. Zarzoso, Numerical validation of the electromagnetic gyrokinetic code NEMORB on global axisymmetric modes, *Nuclear Fusion* 54 (10) (2014) 104004 (oct 2014). doi:10.1088/0029-5515/54/10/104004.

URL <https://doi.org/10.1088/0029-5515/54/10/104004>

- [42] D. Zarzoso, A. Biancalani, A. Bottino, P. Lauber, E. Poli, J.-B. Girardo, X. Garbet, R. Dumont, Analytic dispersion relation of energetic particle driven geodesic acoustic modes and simulations with NEMORB, *Nuclear Fusion* 54 (10) (2014) 103006 (sep 2014). doi:10.1088/0029-5515/54/



[//doi.org/10.1063/1.1351828](https://doi.org/10.1063/1.1351828), doi:10.1063/1.1351828.

URL <https://doi.org/10.1063/1.1351828>

- [51] F. Jenko, W. Dorland, M. Kotschenreuther, B. N. Rogers, Electron temperature gradient driven turbulence, *Phys. Plasmas* 7 (2000) 1904–1910 (May 2000). doi:10.1063/1.874014.
- [52] A. Di Siena, T. Görler, H. Doerk, J. Citrin, T. Johnson, M. Schneider, E. Poli, JET Contributors, Non-Maxwellian background effects in gyrokinetic simulations with GENE, *J. Phys. Conf. Ser.* 775 (2016) 012003 (2016). doi:10.1088/1742-6596/775/1/012003.
- [53] A. Di Siena, T. Görler, H. Doerk, R. Bilato, J. Citrin, T. Johnson, M. Schneider, E. Poli, JET Contributors, Non-Maxwellian fast particle effects in gyrokinetic GENE simulations, *Phys. Plasmas* 25 (2018) 042304 (2018). doi:10.1063/1.5020122.
- [54] A. Di Siena, A. Biancalani, T. Görler, H. Doerk, I. Novikau, P. Lauber, A. Bottino, E. Poli, The ASDEX Upgrade Team, Effect of elongation on energetic particle-induced geodesic acoustic mode, *Nucl. Fusion* 58 (2018) 106014 (2018). doi:10.1088/1741-4326/aad51d.
- [55] T. Görler, X. Lapillonne, S. Brunner, T. Dannert, F. Jenko, F. Merz, D. Told, The global version of the gyrokinetic turbulence code GENE, *Journal of Computational Physics* 230 (2011) 7053–7071 (Aug. 2011). doi:10.1016/j.jcp.2011.05.034.
- [56] T. Dannert, Gyrokinetische Simulation von Plasmaturbulenz mit gefangenen Teilchen und elektromagnetischen Effekten, Ph.D. Thesis, Technische Universität Muenchen (2005).
- [57] T. Dannert, F. Jenko, Gyrokinetic simulation of collisionless trapped-electron mode turbulence, *Phys. Plasmas* 12 (2005) 072309 (2005). doi:10.1063/1.1947447.

- [58] A. Bañón Navarro, P. Morel, M. Albrecht-Marc, D. Carati, F. Merz, T. Görler, F. Jenko, Free energy balance in gyrokinetic turbulence, *Phys. Plasmas* 18 (9) (2011) 092303 (Sep. 2011). doi:10.1063/1.3632077.
- [59] A. Bañón Navarro, P. Morel, M. Albrecht-Marc, D. Carati, F. Merz, T. Görler, F. Jenko, Free Energy Cascade in Gyrokinetic Turbulence, *Phys. Rev. Lett.* 106 (2011) 055001 (2011). doi:10.1103/PhysRevLett.106.055001.
- [60] P. Manas, Y. Camenen, S. Benkadda, W. A. Hornsby, A. G. Peeters, Enhanced stabilisation of trapped electron modes by collisional energy scattering in tokamaks, *Phys. Plasmas* 22 (6) (2015) 062302 (Jun. 2015). doi:10.1063/1.4922754.
- [61] H. Berk, B. Breizman, N. Petviashvili, Spontaneous hole-clump pair creation in weakly unstable plasmas, *Physics Letters A* 234 (3) (1997) 213 – 218 (1997). doi:https://doi.org/10.1016/S0375-9601(97)00523-9.  
URL <http://www.sciencedirect.com/science/article/pii/S0375960197005239>
- [62] H. L. Berk, B. N. Breizman, J. Candy, M. Pekker, N. V. Petviashvili, Spontaneous holeclump pair creation, *Physics of Plasmas* 6 (8) (1999) 3102–3113 (1999). arXiv:https://doi.org/10.1063/1.873550, doi:10.1063/1.873550.  
URL <https://doi.org/10.1063/1.873550>
- [63] H. Berk, C. Boswell, D. Borba, A. Figueiredo, T. Johnson, M. Nave, S. Pinches, S. Sharapov, J. E. contributors, Explanation of the JETn=0 chirping mode, *Nuclear Fusion* 46 (10) (2006) S888–S897 (sep 2006). doi:10.1088/0029-5515/46/10/s04.  
URL <https://doi.org/10.1088/0029-5515/46/10/s04>
- [64] H. Berk, C. Boswell, D. Borba, A. Figueiredo, T. Johnson, M. Nave, S. Pinches, S. Sharapov, J. E. contributors, Explanation of the JETn=

0 chirping mode, erratum, Nuclear Fusion 50 (4) (2010) 049802 (apr 2010).  
doi:10.1088/0029-5515/50/4/049802.

URL <https://doi.org/10.1088/0029-5515/50/4/049802>

- [65] H. Wang, Y. Todo, C. C. Kim, Hole-clump pair creation in the evolution of energetic-particle-driven geodesic acoustic modes, Phys. Rev. Lett. 110 (2013) 155006 (Apr 2013). doi:10.1103/PhysRevLett.110.155006.

URL <https://link.aps.org/doi/10.1103/PhysRevLett.110.155006>

- [66] A. Biancalani, I. Chavdarovski, Z. Qiu, A. Bottino, D. Del Sarto, A. Ghizzo, Ö. D. Gürçan, P. Morel, I. Novikau, Saturation of energetic-particle-driven geodesic acoustic modes due to waveparticle nonlinearity, Journal of Plasma Physics 83 (6) (2017) 725830602 (2017). doi:10.1017/S0022377817000976.

- [67] T. C. Li, G. G. Howes, K. G. Klein, J. M. TenBarge, ENERGY DISSIPATION AND LANDAU DAMPING IN TWO- AND THREE-DIMENSIONAL PLASMA TURBULENCE, The Astrophysical Journal 832 (2) (2016) L24 (nov 2016). doi:10.3847/2041-8205/832/2/L24.

URL <https://doi.org/10.3847/2041-8205/832/2/L24>

- [68] T. N. Parashar, W. H. Matthaeus, M. A. Shay, Dependence of kinetic plasma turbulence on plasma  $\beta$ , The Astrophysical Journal 864 (1) (2018) L21 (aug 2018). doi:10.3847/2041-8213/aadb8b.

URL <https://doi.org/10.3847/2041-8213/aadb8b>

- [69] S. Du, F. Guo, G. P. Zank, X. Li, A. Stanier, Plasma energization in colliding magnetic flux ropes, The Astrophysical Journal 867 (1) (2018) 16 (oct 2018). doi:10.3847/1538-4357/aae30e.

URL <https://doi.org/10.3847/1538-4357/aae30e>

- [70] R. A. Cairns, Plasma Physics, p. 104, Dordrecht Springer Netherlands, 1985.

URL <http://dx.doi.org/10.1007/978-94-010-9655-3?nosfx=y>

- [71] F. W. King, Hilbert Transforms, Vol. 2, p. 465, Cambridge Cambridge University Press, 2009.  
URL <https://doi.org/10.1017/CB09780511735271>